Appropriate Window Function and Window Length in Multifrequency Velocity Estimator for Rapid Motion and Locality of Layered Myocardium

Yu Obara, Shohei Mori, *Member, IEEE*, Mototaka Arakawa, *Member, IEEE*, and Hiroshi Kanai, *Senior Member, IEEE*

***Abstract*— The heart wall has a multilayered structure and moves rapidly during ejection and rapid filling periods. Local strain rate (SR) measurements of each myocardial layer can contribute to accurate and sensitive evaluations of myocardial function. However, ultrasound-based velocity estimators using a single-frequency phase difference cannot realize these measurements owing to insufficient maximum detectable velocity, which is limited by a quadrature frequency. We previously proposed a velocity estimator using multifrequency phase differences to improve the maximum detectable velocity. However, the improvement is affected by a spatial discrete Fourier transform (DFT) window length that represents the locality of the velocity estimation. In this article, we theoretically describe that shortening the window increases the interference between different frequency components and decreases the maximum detectable velocity. The tradeoff between the maximum detectable velocity and the window length was confirmed through simulations and a water-tank experiment. Under the tradeoff, the Hanning window, which was used in previous studies, is not always appropriate for the local measurement of the velocity, which sometimes exceeds 100 mm/s depending on the subject, direction of the ultrasound beam to the heart wall, and cardiac periods. In the *in vivo* measurement with the short window, the Tukey window with a large flat part that has a high-frequency resolution and ameliorates the discontinuity at both edges of the windowed signal was appropriate to measure the maximum velocity. This study offers the potential for local measurements of each myocardial layer using the multifrequency velocity estimator with the appropriate window function and window length.**

***Index Terms*— Aliasing, discrete Fourier transform (DFT), multifrequency phase differences, velocity measurement, window function, window length.**

Manuscript received December 27, 2021; accepted February 17, 2022. Date of publication February 21, 2022; date of current version March 28, 2022. This work was supported in part by the Japan Society for the Promotion of Science KAKENHI under Grant 20H02156 and Grant 19K22943, and in part by the Ministry of Education, Culture, Sports, Science and Technology, University Fellowship Funding Project for Innovation Creation in Science and Technology. *(Corresponding author: Yu Obara.)*

This work involved human subjects or animals in its research. Approval of all ethical and experimental procedures and protocols was granted by the Ethics Committee of the Graduate School of Engineering, Tohoku University, Sendai, Japan, under Approval No. 08A-2.

Yu Obara is with the Graduate School of Biomedical Engineering, Tohoku University, Sendai 9808579, Japan (e-mail: yu.obara.s2@dc.tohoku.ac.jp).

Shohei Mori is with the Graduate School of Engineering, Tohoku University, Sendai 9808579, Japan (e-mail: shohei.mori.a2@tohoku.ac.jp).

Mototaka Arakawa and Hiroshi Kanai are with the Graduate School of Biomedical Engineering and the Graduate School of Engineering, Tohoku University, Sendai 9808579, Japan (e-mail: mototaka.arakawa.c3@tohoku.ac.jp; hiroshi.kanai.e7@tohoku.ac.jp).

Digital Object Identifier 10.1109/TUFFC.2022.3153048

I. Introduction

MYOCARDIAL ischemia leads to ischemic heart diseases, such as myocardial infarction and angina, which are the main causes of death worldwide [1]. Myocardial ischemia in the early stages can be repaired using reperfusion therapy. It is, therefore, important to detect it at an early stage. Because it occurs in the subendocardial region of the heart wall and progresses transmurally toward the subepicardial region [2]–[4], the local evaluation of myocardial function in the transmural direction can be useful for its detection.

Ultrasound-based measurements of strain rate (SR) have been introduced to noninvasively evaluate regional myocardial function [5]–[8]. The myocardial SR, in which the whole motion of the heart wall is removed, represents an instantaneous change in the myocardial thickness. Previous studies have suggested that myocardial SR can assess an acutely ischemic myocardium [9]–[12]. Because the heart wall has a multilayered structure, local SR measurements of each myocardial layer can contribute to the highly accurate and sensitive evaluations of myocardial function.

Moreover, the SR distribution has the potential to reveal the mechanism of the transition process in the myocardium from relaxation to contraction. In our previous studies, the propagation of the contractile response caused by the conduction of electrical excitation was measured using a velocity waveform [13]–[15] or an SR distribution of the myocardium [16]–[18]. Because the whole motion of the heart wall is removed in the SR measurement, it may be useful for measuring the propagation of the local and minute contractile responses [18], thereby contributing to the detailed elucidation

of the transition process in the myocardium from relaxation to contraction.

The myocardial SR distribution has been calculated from the velocities at multiple positions in the heart wall. In addition, the velocities in the heart wall are useful for understanding whether the heart wall motion is related to the measured SR. Thus, velocity estimation is important for SR measurement. A velocity-estimation method based on the phase differences between consecutive frames has been developed for measuring the velocities in the heart wall [19], [20]. This method uses the phase differences between consecutive frames in the demodulated signals and estimates the subpixel displacements without interpolation. Thus, this method is computationally inexpensive compared to the block matching method [21] and has been applied for real-time SR imaging [6], [22].

The maximum detectable velocity in this method, which is based on the phase difference of a single frequency, is limited and depends on the quadrature frequency. The maximum detectable velocity may sometimes be insufficient to measure the rapid motion of the heart wall, especially during the ejection and rapid filling periods. In these cases, aliasing occurs in the velocity waveform even when the frame rate is set to several hundreds of Hz. Although the aliasing often occurs in the normal myocardium rather than the ischemic myocardium because the velocity decreases owing to the myocardial ischemia, the aliasing is a problem to detect the abnormality owing to the myocardial ischemia because the large velocity in the normal myocardium has to be correctly measured as a reference.

To overcome this problem, several studies have proposed anti-aliasing techniques based on the multifrequency phase differences between two consecutive frames [23]–[25]. The improvement of the maximum detectable velocity in the measurement of blood flow by a large spatial window has already been confirmed [23]–[25]. To estimate the velocity in the heart wall, we previously proposed a multifrequency phased-tracking method [26] that achieves a larger maximum detectable velocity than that achievable using a single-frequency phase difference.

The key factor that determines the maximum detectable velocity in measurements based on the multifrequency phase differences is the length of the spatial window. The multifrequency phase differences should be measured independently for each frequency component. However, a short spatial window that has a poor frequency resolution makes such measurements difficult. Thus, the improvement of the maximum detectable velocity is negatively affected when the spatial window for the velocity estimation is shortened.

By contrast, the local SR measurement in the heart wall requires the local velocity to be estimated with a short spatial window. The heart wall has a large velocity component related to its whole motion and a minute velocity component caused by the local change in the thickness of the myocardial layer. Because the velocity estimation assumes that the velocities are uniform within the spatial window, it is difficult to measure the minute velocity caused by the local change in the thickness of the myocardial layer using a long spatial window. A previous study confirmed that the spatial window length affects the SR distribution in a layered myocardium [27].

There is a tradeoff between the maximum detectable velocity and the window length in a velocity estimation based on the multifrequency phase differences. Thus, the influence of the window length of the velocity estimation on the maximum detectable velocity should be validated to determine the appropriate spatial window for the local SR measurement based on the multifrequency phase differences. The purpose of this study is to elucidate the relationship between the maximum detectable velocity and the window length in the velocity estimation. Therefore, we validate the relationship through simulations and a water-tank experiment. We then discuss the tradeoff between the maximum detectable velocity and the length of the spatial window and present an appropriate window function for the rapid motion and locality of the layered myocardium through an *in vivo* experiment.

II. Principles

A. Velocity Estimation Based on Single-Frequency Phase Difference

The displacement $\Delta z(n)$ between the nth and the $(n+\Delta n)$th frames leads to a delay time between the received radio frequency (RF) signals, $s(t; n)$ and $s(t; n + \Delta n)$, in the same ultrasound beam. The delay time $\tau(n)$ is given by

$$\tau(n) = \frac{2 \cdot \Delta z(n)}{c_0} \tag{1}$$

where c_0 is the speed of sound.

The demodulated signals are obtained by applying quadrature demodulation with the carrier frequency f to the RF signals. The phase difference $\Delta\theta_f(n)$ between the demodulated signals is

$$\Delta\theta_f(n) = -2\pi f \cdot \tau(n) = -4\pi f \frac{\Delta z(n)}{c_0}. \tag{2}$$

In digital signal processing, this phase difference $\Delta\theta_f(n)$ can be calculated from the cross-spectrum between the nth and the $(n + \Delta n)$th frames [28]. The spectra $S(f; n)$ and $S(f; n + \Delta n)$ are obtained by applying discrete Fourier transform (DFT) to the windowed signals. The cross-spectrum $C(f; n)$ between the frames is given by

$$C(f; n) = S^*(f; n) \cdot S(f; n + \Delta n) \tag{3}$$

where $*$ denotes complex conjugation.

The phase of the cross-spectrum $\angle C(f; n)$ is the phase difference $\Delta\theta_f(n)$ between the demodulated signals with the carrier frequency f. In a previous study, it was confirmed that the phase of the cross-spectrum at the center frequency f_c should be used to estimate the minute velocity accurately [28]. Thus, the average velocity between frames is estimated using $\angle C(f_c; n)$ as

$$\hat{v}_{f_c}(n) = -\frac{c_0 f_{FR}}{4\pi} \cdot \frac{\angle C(f_c; n)}{f_c}. \tag{4}$$

Here, f_{FR} is the frame rate.

If the amplitude of the phase difference exceeds π, that is, the delay time caused by the displacement exceeds half

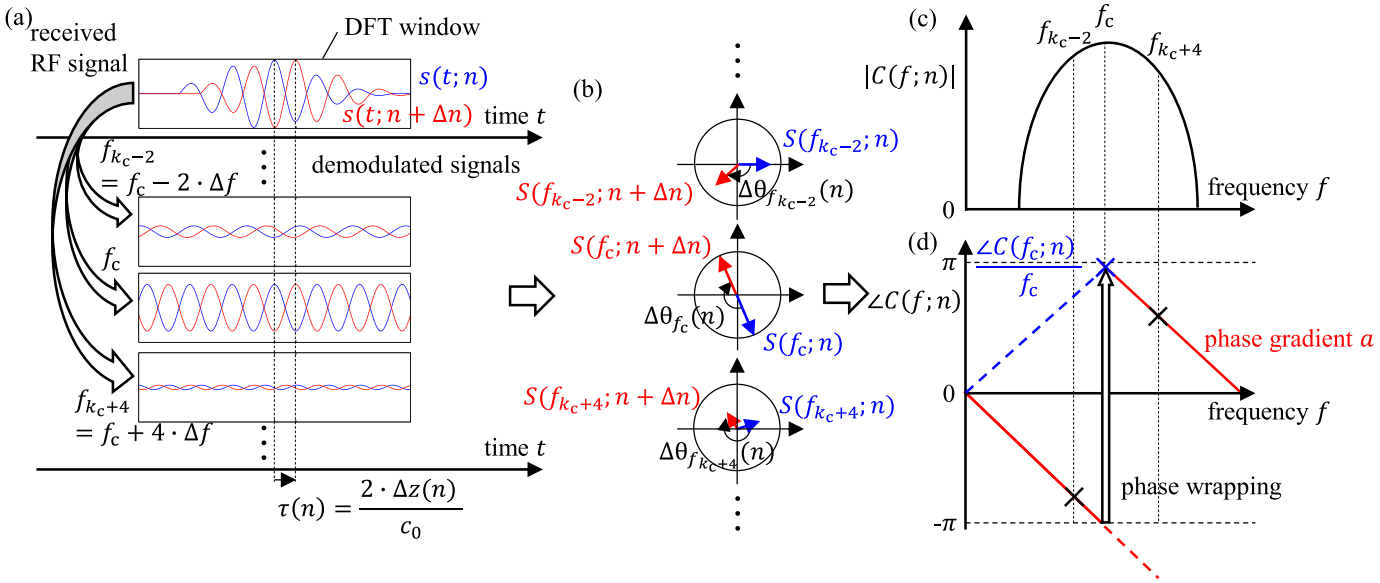

Fig. 1. Schematic of the velocity estimation based on multifrequency phase differences. (a) Received RF signals and their demodulated signals at the nth and the $(n+\Delta n)$th frames. (b) Frequency components of the spectra of the received RF signals. (c) Amplitude of the cross spectrum between the nth and the $(n+\Delta n)$th frames. (d) Phase of the cross spectrum. Δf representing the frequency interval in the spectrum obtained by DFT.

the period of the center frequency f_c, then the phase of the cross-spectrum is wrapped and aliasing occurs. Aliasing causes a large displacement error. By substituting π into $\angle C(f_c;n)$ in (4), the maximum detectable velocity $|\hat{v}_{f_c,\mathrm{MAX}}|$ and displacement $|\widehat{\Delta z}_{f_c,\mathrm{MAX}}|$ based on the single-frequency phase difference are given by

$$\left|\hat{v}_{f_c,\mathrm{MAX}}\right| = \left|\widehat{\Delta z}_{f_c,\mathrm{MAX}}\right| \cdot f_{\mathrm{FR}} = \frac{c_0}{4f_c} \cdot f_{\mathrm{FR}}. \tag{5}$$

B. Velocity Estimation Based on Multifrequency Phase Differences

Fig. 1 schematically illustrates the velocity estimation based on multifrequency phase differences. Assuming that the displacement from the nth frame to the $(n+\Delta n)$th frame, $\Delta z(n)$, is spatially uniform in the DFT window, the phase difference is linearly proportional to the carrier frequency, according to (2). Thus, the gradient of the phase difference a_n is expressed as

$$a_n = -\frac{4\pi}{c_0}\Delta z(n). \tag{6}$$

This is estimated using the cross-spectrum phase. The phase gradient of the cross-spectrum is estimated using the weighted least-squares method to ameliorate the negative effects of the attenuation and interference of backscattered waves from multiple scatterers in the myocardium in the velocity estimation [26]. The root mean squared error (RMSE) α_n of the phase of the cross-spectrum, weighted by the amplitude of the cross-spectrum, is defined with the arbitrary variable a as follows:

$$\alpha_n(a) = \sqrt{\frac{\sum_{f=0}^{f_s/2}|C(f;n)|\cdot\delta_f^2(a)}{\sum_{f=0}^{f_s/2}|C(f;n)|}} \tag{7}$$

$$\delta_f^2(a) = \min_m\left(|\angle C(f;n) - af + 2\pi m|^2\right). \tag{8}$$

Here, f_s is the sampling frequency and m is an arbitrary integer. Because the phase of the cross-spectrum is within the range of $[-\pi,\pi]$, the phase af must also fall within the same range. When the value of af falls outside this range, 2π is subtracted from or added to the value of af to handle the wrapped phase.

From (6), the average velocity $\hat{v}(n)$ between the frames is expressed in terms of the estimated phase gradient $\hat{a}_n$ as

$$\hat{v}(n) = \widehat{\Delta z}\cdot f_{\mathrm{FR}} = -\frac{c_0 f_{\mathrm{FR}}}{4\pi}\cdot\hat{a}_n \tag{9}$$

$$\hat{a}_n = \arg\min_a \alpha_n(a). \tag{10}$$

As shown in Fig. 1(d), the phase gradient can be estimated based on the multifrequency phase differences even when the phase wraps at the center frequency. However, the phase gradient based on the single-frequency phase difference in (4), $\angle C(f_c;n)/f_c$, does not correspond to the true phase gradient. The multifrequency phase differences allow us to measure large velocities that cannot be measured using only the single-frequency phase difference.

The phase gradient cannot be estimated when the change in the phase of the cross-spectrum between adjacent frequency components exceeds π. Thus, delay times that exceed half the period of the DFT window in the time domain cannot be detected from the cross-spectrum phase. The frequency interval Δf of the cross-spectrum phase is determined by the length of the DFT window L_{DFT} as follows:

$$\Delta f = \frac{c_0}{2\cdot L_{\mathrm{DFT}}}. \tag{11}$$

Thus, the maximum phase gradient $|\hat{a}_{\mathrm{MAX}}|$, displacement $|\widehat{\Delta z}_{\mathrm{MAX}}|$, and velocity $|\hat{v}_{\mathrm{MAX}}|$ limited by the frequency interval

Δf are given by

$$|\hat{a}_{\mathrm{MAX}}| = \frac{\pi}{\Delta f} = \frac{2\pi \cdot L_{\mathrm{DFT}}}{c_0} \tag{12}$$

$$|\hat{v}_{\mathrm{MAX}}| = |\widehat{\Delta z}_{\mathrm{MAX}}| \cdot f_{\mathrm{FR}} = \frac{L_{\mathrm{DFT}}}{2} \cdot f_{\mathrm{FR}}. \tag{13}$$

This maximum velocity $|\hat{v}_{\mathrm{MAX}}|$ is usually larger than the maximum velocity $|\hat{v}_{f_c,\mathrm{MAX}}|$ that can be detected based on the single-frequency phase difference because the length of the DFT window L_{DFT} should be set to be longer than half the wavelength at the center frequency f_c [28].

C. Formulization of Multifrequency Phase Differences Measured With DFT Window

In both the single-frequency and multifrequency phase difference methods, it is assumed that the phase difference at each frequency component is independent of the others, that is, there is no interference between different frequency components. When this assumption is correct, the maximum detectable velocity based on the multifrequency phase differences corresponds to the maximum velocity $|\hat{v}_{\mathrm{MAX}}|$ limited by the frequency interval in (13).

In practice, however, there is interference between the different frequency components because both the bandwidth of the received RF signal and the length of the window are finite. Interference between the different frequency components should be considered, especially for local measurements. Shortening the spatial DFT window improves the locality of the velocity estimation. However, it also results in poorer frequency resolution and makes the independent measurement of each frequency component difficult. The assumption that there is no interference between different frequency components then becomes incorrect. In this case, the maximum detectable velocity based on the multifrequency phase differences becomes smaller than the maximum velocity $|\hat{v}_{\mathrm{MAX}}|$ limited by the frequency interval in (13), as the DFT window becomes shorter.

We formulized the measured cross-spectrum phase (i.e., the multifrequency phase differences) obtained by DFT to capture the influence of the interference between different frequency components on the maximum detectable velocity in the velocity estimation based on the multifrequency phase differences. In this section, a very simple model without any noise is introduced to evaluate only the influence of the interference between different frequency components on the velocity estimation based on the multifrequency phase differences. The pulse wave representing the impulse response $h(t)$ of the ultrasound transducer is often approximated as the product of a cosine wave at the center frequency f_c with the Gaussian function as

$$h(t) = e^{-t^2/\sigma^2} \cdot \cos(2\pi f_c t). \tag{14}$$

Here, $t = l/f_s (l = 0, 1, 2, \ldots)$ is a discrete time and σ is the standard deviation of the Gaussian function. When there is a single point scatterer on the ultrasound beam, the received RF signal $s_m(t; n)$ is expressed according to the convolution model

$$\begin{aligned} s_m(t; n) &= A_0 \cdot h(t - t_n) \\ &= A_0 \cdot e^{-(t-t_n)^2/\sigma^2} \cdot \cos(2\pi f_c(t - t_n)). \end{aligned} \tag{15}$$

Here, A_0 is the reflectance of the scatterer and t_n is the two-way propagation time from the ultrasound probe to the scatterer in the nth frame.

The true spectrum without the influence of windowing is obtained by applying a discrete-time Fourier transform to the infinite-length modeled RF signal. The true spectrum $S_m(f; n)$ of the infinite-length modeled RF signal is given by the convolution of the cosine wave at the center frequency f_c and the Gaussian function in the frequency domain as follows:

$$\begin{aligned} S_m(f; n) &= A_0 \cdot e^{-\sigma^2(f-f_c)^2} \cdot e^{-j2\pi t_n f} \\ &= |S_m(f; n)| \cdot e^{-j2\pi t_n f}. \end{aligned} \tag{16}$$

From (3) and (16), the true cross-spectrum $C_m(f; n)$ between the true spectra $S_m(f; n)$ and $S_m(f; n + \Delta n)$ at the nth and $(n + \Delta n)$th frames, respectively, is expressed as

$$\begin{aligned} C_m(f; n) &= A_0 e^{-\sigma^2(f-f_c)^2} e^{j2\pi t_n f} \cdot A_0 e^{-\sigma^2(f-f_c)^2} e^{-j2\pi(t_n+\tau(n))f} \\ &= |S_m(f; n)|^2 \cdot e^{-j2\pi\tau(n)f}. \end{aligned} \tag{17}$$

Here, $\tau(n)$ is the delay time generated by the displacement from the nth frame to the $(n + \Delta n)$th frame. In the true cross-spectrum phase $\angle C_m(f; n)$, only the delay time component $e^{-j2\pi\tau(n)f}$ remains because the propagation time component $e^{-j2\pi t_n f}$ cancels out. Thus, $\angle C_m(f; n)$ is linearly proportional to the frequency f, as seen in (2).

The spectrum obtained by DFT using a finite-length window is expressed as the convolution of the true spectrum $S_m(f; n)$ and the window function spectrum $W(f)$. Thus, the measured spectrum obtained by DFT, $S'_m(f_k; n)$, is expressed as

$$S'_m(f_k; n) = (S_m(f; n) * W(f))|_{f=f_k} \tag{18}$$

$$f_k = k \cdot \Delta f \tag{19}$$

where f_k is a discrete frequency and k is an integer. The range of the discrete frequency f_k is $[-f_s/2 : f_s/2]$. In this article, the integer k in (19) is defined as k_c when $f_{k_c} = f_c$.

Most of the window functions used for the DFT, such as the Hanning window, are even functions. In this case, the phase $\angle W_0(f)$ of the window function spectrum, in which the center point is set at the origin, has a zero-phase characteristic. Thus, the spectrum of the window function $W(f)$ has only the linear phase component $e^{-j2\pi t_n f}$, which is relevant to the center point of the window function set at the time t_n, and the phase $\angle W(f)$, which is proportional to the frequency f. The spectrum of the window function $W(f)$ is given by

$$W(f) = W_0(f) \cdot e^{-j2\pi t_n f}. \tag{20}$$

From (18)–(20), the measured spectrum at the nth frame $S'_m(f_k; n)$ that is obtained by DFT, is expressed as follows:

$$\begin{aligned} S'_m(f_k; n) &= \int_{-\infty}^{+\infty} S_m(f; n) \cdot W(f_k - f) df \\ &= e^{-j2\pi t_n f_k} \int_{-\infty}^{+\infty} |S_m(f; n)| \cdot W_0(f_k - f) df \\ &= \left|S'_m(f_k; n)\right| \cdot e^{-j2\pi t_n f_k}. \end{aligned} \tag{21}$$

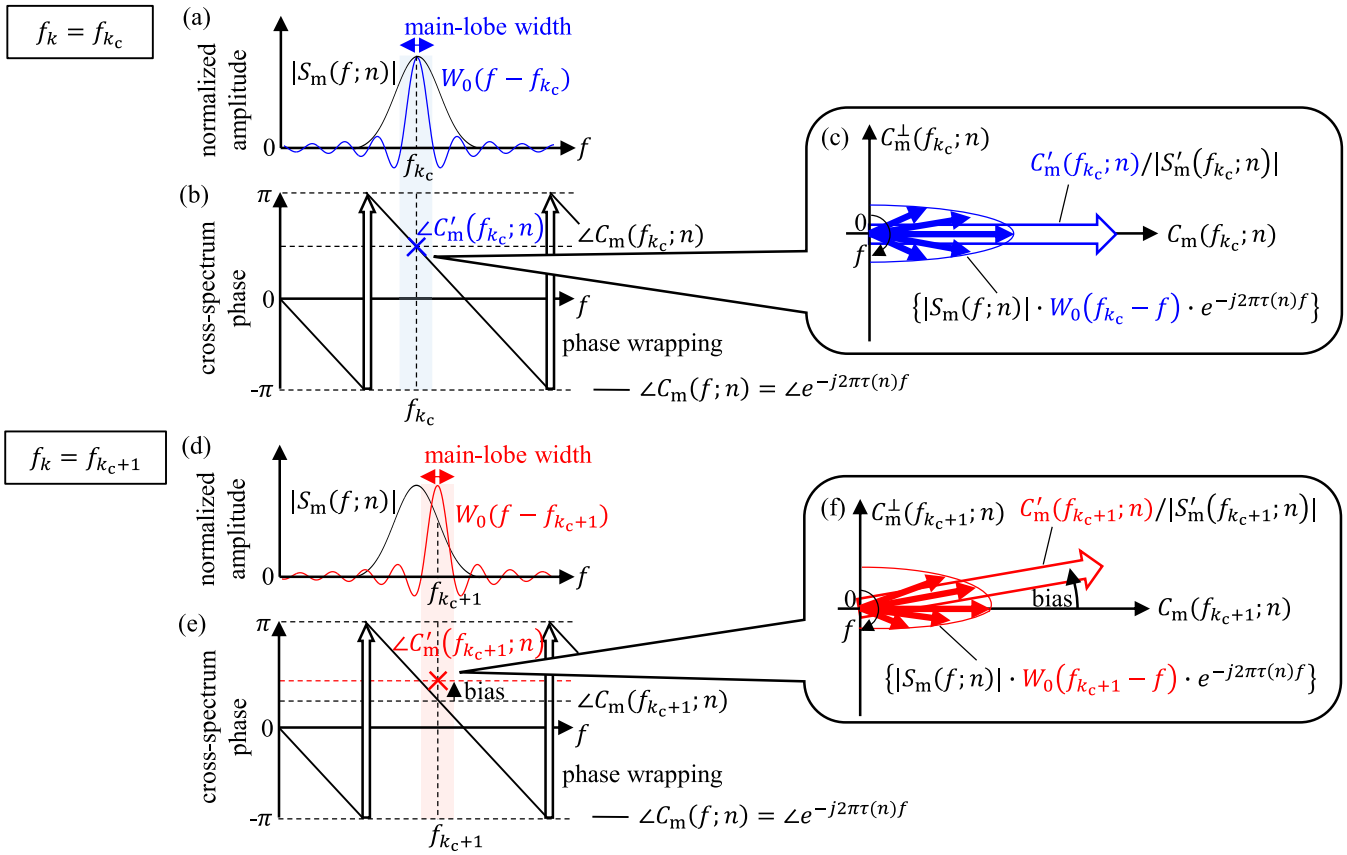

Fig. 2. (a) Amplitude of the spectrum of the modeled RF signal $|S_m(f;n)|$ and that of the window function spectrum $W_0(f - f_{k_c})$ convoluted at the center frequency. (b) Phase of the true cross-spectrum $\angle C_m(f;n)$ and that of the measured cross-spectrum $\angle C'_m(f_{k_c};n)$ at the center frequency. (c) Schematic of the summation of the delay time components $e^{-j2\pi\tau(n)f}$ in $\angle C'_m(f_{k_c};n)$. (d) Amplitude of the spectrum of the modeled RF signal $|S_m(f;n)|$ and that of the window function spectrum $W_0(f - f_{k_c+1})$, convoluted at the adjacent frequency to the center frequency. (e) Phase of the true cross-spectrum $\angle C_m(f;n)$ and that of the measured cross-spectrum $\angle C'_m(f_{k_c+1};n)$ at the adjacent frequency to the center frequency. (f) Schematic of the summation of the delay time components $e^{-j2\pi\tau(n)f}$ in $\angle C'_m(f_{k_c+1};n)$. Note the location of the mainlobe of the window function is not centered with the bandwidth of $|S_m(f;n)|$ when the frequency f_k to be calculated does not correspond to the center frequency f_c.

When the center point of the window function does not change between the nth and the $(n + \Delta n)$th frames, the measured spectrum at the $(n + \Delta n)$th frame $S'_m(f_k; n + \Delta n)$, which is obtained by DFT, is expressed as follows:

$$S'_m(f_k; n + \Delta n) = e^{-j2\pi t_n f_k} \int_{-\infty}^{+\infty} |S_m(f;n)| \cdot W_0(f_k - f) \cdot e^{-j2\pi\tau(n)f} df. \quad (22)$$

From (3) and (22), the measured cross-spectrum $C'_m(f_k;n)$ between $S'_m(f_k;n)$ and $S'_m(f_k;n+\Delta n)$ is expressed as follows:

$$\begin{aligned} &C'_m(f_k;n) \\ &= |S'_m(f_k;n)| \cdot e^{+j2\pi t_n f_k} \\ &\quad \cdot e^{-j2\pi t_n f_k} \left(\int_{-\infty}^{+\infty} |S_m(f;n)| \cdot W_0(f_k - f) \cdot e^{-j2\pi\tau(n)f} df \right) \\ &= |S'_m(f_k;n)| \cdot \left(\int_{-\infty}^{+\infty} |S_m(f;n)| \cdot W_0(f_k - f) \cdot e^{-j2\pi\tau(n)f} df \right). \end{aligned} \quad (23)$$

Thus, the phase of the measured cross-spectrum $\angle C'_m(f_k;n)$ corresponds to the phase of the sum of the delay time component $e^{-j2\pi\tau(n)f}$ weighted by $|S_m(f;n)| \cdot W_0(f_k - f)$. The measured cross-spectrum phase $\angle C'_m(f_k;n)$ is formulized as follows:

$$\angle C'_m(f_k;n) = \angle \left(\int_{-\infty}^{+\infty} |S_m(f;n)| \cdot W_0(f_k - f) \cdot e^{-j2\pi\tau(n)f} df \right). \quad (24)$$

D. Influence of the Window Length of the Velocity Estimation Based on Multifrequency Phase Differences on the Maximum Detectable Velocity

Fig. 2 schematically illustrates the influence of the interference between different frequency components on the measured cross-spectrum phase used in the velocity estimation. Fig. 2(a) illustrates the amplitude of the true spectrum $|S_m(f;n)|$ and that of the window function $W_0(f - f_{k_c})$ shifted by the center frequency. In Fig. 2(a), the mainlobe width corresponds to the frequency resolution of the window function. Fig. 2(b) illustrates the phase of the true cross-spectrum $\angle C_m(f;n)$ and that of the measured cross-spectrum at the center frequency, $\angle C'_m(f_{k_c};n)$.

Fig. 2(c) schematically illustrates the summation of the weighted delay time components $|S_m(f;n)| \cdot W_0(f_{k_c} - f) \cdot e^{-j2\pi\tau(n)f}$ (blue vectors) at $f_k = f_{k_c} = f_c$, where both

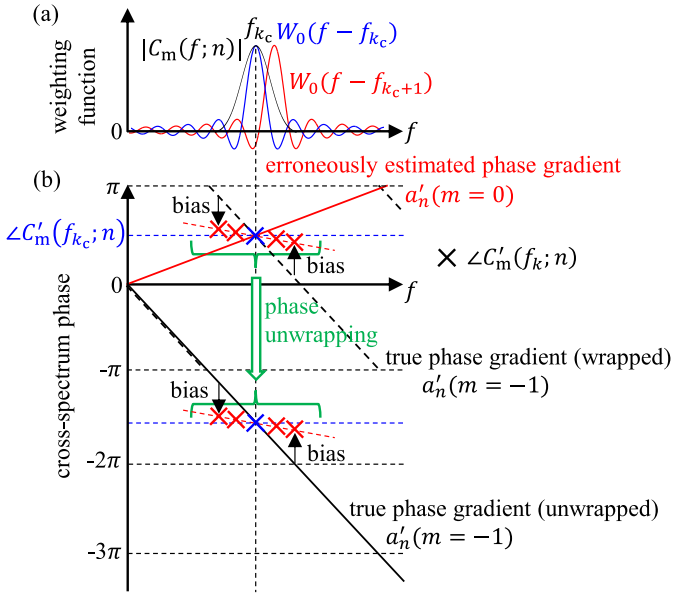

Fig. 3. (a) Amplitude of the cross-spectrum $|C_m(f;n)|$ and that of the window functions $W_0(f-f_{k_c})$ and $W_0(f-f_{k_c+1})$. (b) Wrapped true phase gradient, the unwrapped true phase gradient, the erroneously estimated phase gradient, and the phase of the measured cross-spectrum, $\angle C'_m(f_k;n)$. Note that both the wrapped, and the unwrapped measured cross spectrum $\angle C'_m(f_k;n)$ are illustrated.

$|S_m(f;n)|$ and $W_0(f-f_{k_c})$ are symmetric with respect to the center frequency f_c, as shown in black and blue in Fig. 2(a). Thus, as shown in Fig. 2(c), the phase of the sum of the weighted delay time components, $\angle(C'_m(f_{k_c};n)/|S'_m(f_{k_c};n)|)$, (white vector) corresponds to the true value $\angle C_m(f_c;n)$ at the center frequency f_c. The phase of the measured cross-spectrum $\angle C'_m(f_{k_c};n)$, therefore, coincides with the true phase $\angle C_m(f_c;n)$ in principle, as theoretically confirmed by Hasegawa and Kanai [28].

Fig. 2(d) illustrates the amplitude of the true spectrum $|S_m(f;n)|$ and that of the window function $W_0(f-f_{k_c+1})$ shifted by the frequency f_{k_c+1} adjacent to the center frequency f_{k_c}. Fig. 2(e) illustrates the phase of the true cross-spectrum $\angle C_m(f;n)$ and that of the measured cross-spectrum $\angle C'_m(f_{k_c+1};n)$. Fig. 2(f) schematically illustrates the summation of the weighted delay time components $|S_m(f;n)|\cdot W_0(f_{k_c+1}-f)\cdot e^{-j2\pi\tau(n)f}$ (red vectors), when $f_k=f_{k_c+1}>f_c$. $W_0(f-f_{k_c+1})$ is symmetric with respect to the discrete frequency f_{k_c+1}, as shown in red in Fig. 2(d). However, $|S_m(f;n)|$ is asymmetric with respect to the discrete frequency f_{k_c+1}, as shown in black in Fig. 2(d). Thus, a bias error occurs in the phase of the measured cross-spectrum $\angle C'_m(f_{k_c+1};n)$, as shown in Fig. 2(e). As shown in Fig. 2(f), positive bias errors occur when $f_k>f_c$. Conversely, the bias error values are negative when $f_k<f_c$. The amount of bias error in the phase of the measured cross-spectrum depends mainly on the mainlobe width of the window function $W_0(f-f_k)$ (i.e., the length of the spatial window) compared with the bandwidth of the true spectrum $S_m(f;n)$ and the true phase gradient (i.e., the delay time $\tau(n)$ generated by the displacement between the frames). Because the velocity is estimated from the phase gradient, the amount of bias error also depends on the velocity.

Fig. 3 schematically illustrates the influence of the bias errors in the measured cross-spectrum phases on the velocity estimation based on the multifrequency phase differences. Fig. 3(a) illustrates the amplitude of the cross-spectrum $|C_m(f;n)|$ and that of the window functions $W_0(f-f_{k_c})$ and $W_0(f-f_{k_c+1})$. Fig. 3(b) illustrates the wrapped true phase gradient, the unwrapped true phase gradient, the erroneously estimated phase gradient, and the phase of the measured cross-spectrum $\angle C'_m(f_k;n)$.

When the measured cross-spectrum amplitude $|C'_m(f_k;n)|$ is used as the weight to estimate the phase gradient, as shown in (7)–(10), the measured phase at the center frequency $\angle C'_m(f_{k_c};n)$ is dominant over those at other frequencies. The measured cross-spectrum phase coincides with the true phase at the center frequency. The possible values of the phase gradient a'_n that passes through the origin and the phase at the center frequency are expressed as

$$a'_n(m)=\frac{\angle C_m(f_c;n)}{f_c}+\frac{2\pi m}{f_c}. \tag{25}$$

Here, m is an arbitrary integer and the second term on the right side of the equation accounts for the wrapped phase in the true cross-spectrum phase at the center frequency, $\angle C_m(f_c;n)$. The absolute value of m represents the number of phase wraps in $\angle C_m(f_k;n)$ in the range of $f_k\le f_c$. For example, $m=-1$ means that the phase of the cross-spectrum is wrapped once from a negative value to a positive value in the range of $f_k\le f_c$, as shown in Fig. 3(b).

When the bias errors are large, the apparent gradient of the measured phase of the cross-spectrum (red dashed line) is smaller than the true phase gradient (black lines) around the center frequency, as shown in Fig. 3(b). In this case, the bias errors increase the weighted RMSE at the true phase gradient $a'_n(-1)$ and decrease that at $a'_n(0)$. Thus, the weighted RMSE is minimum at $a'_n(0)$ (red solid line) even though the true phase gradient is $a'_n(-1)$, and an erroneous phase gradient is estimated. The large displacement error caused by this erroneous estimation of m has the same effect as that caused by aliasing at the center frequency in the velocity estimation based on a single-frequency phase difference. Therefore, the maximum detectable velocity becomes smaller than the maximum velocity limited by the frequency interval $|\hat{v}_{MAX}|$ in (13), owing to the bias errors caused by the interference between different frequency components.

E. Influence of Noise on the Maximum Detectable Velocity Based on Multifrequency Phase Differences

If noise presents, it causes a variance in the measured cross-spectrum phase at each discrete frequency even if there is no interference between different frequency components. Fig. 4 schematically illustrates the influence of the noise variance in the measured cross-spectrum phase on the velocity estimation based on the multifrequency phase differences when the frequency resolution is sufficiently high. Fig. 4(a) illustrates the amplitude of the cross-spectrum $|C_m(f;n)|$ and that of the window functions $W_0(f-f_{k_c})$ and $W_0(f-f_{k_c+1})$. Fig. 4(b) illustrates the wrapped true phase gradient, the erroneously

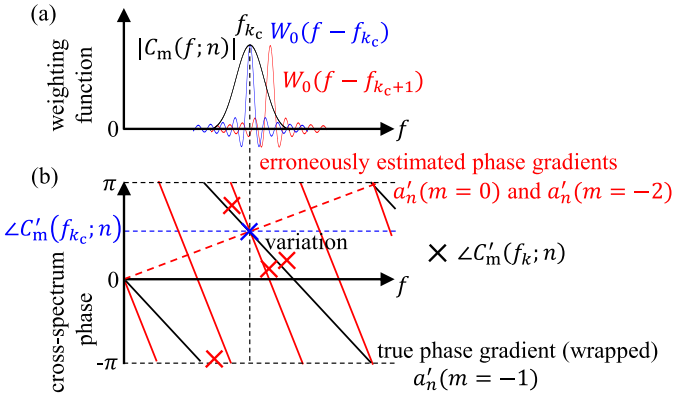

Fig. 4. (a) Amplitude of the cross-spectrum $|C_m(f;n)|$ and that of the window functions $W_0(f-f_{k_c})$ and $W_0(f-f_{k_c+1})$. (b) Wrapped true phase gradient, the wrapped erroneously estimated phase gradients $a'_n(0)$ and $a'_n(-2)$, and the phase of the measured cross-spectrum $\angle C'_m(f_k;n)$. Note that there are only a few bias errors in the measured cross-spectrum phases because the frequency resolution is sufficiently high.

estimated phase gradients, and the phase of the measured cross-spectrum $\angle C'_m(f_k;n)$.

If the noise variance is minimum at the center frequency where the cross-spectrum amplitude $|C_m(f;n)|$ is maximum, its influence in the measured cross-spectrum phase on the possible phase gradients $a'_n(m)$ in (25) can be ameliorated by the weight of the measured cross-spectrum amplitude $|C'_m(f_k;n)|$. However, the noise variance at a frequency other than the center frequency may increase the weighted RMSE at the true phase gradient $a'_n(-1)$ and decrease that at $a'_n(-2)$, as shown in Fig. 4(b). In this case, the noise variance in the measured cross-spectrum phase causes the erroneous estimation of m in the possible phase gradients $a'_n(m)$, and the phase gradient is erroneously estimated as $a'_n(-2)$. Thus, the large displacement error of half the wavelength at the center frequency occurs as an aliasing error. Depending on the noise variance, the phase gradient may be erroneously estimated as not only $a'_n(-2)$ but also $a'_n(0)$, $a'_n(1)$, $a'_n(-3)$, or the others with the erroneous value of m. The large noise components may cause an aliasing error even though the frequency resolution of the DFT window is high enough to measure each frequency component independently.

If the noise is regarded as white noise, the noise variance in the measured spectrum can be alleviated by elongating the DFT window [29], [30]. In practice, however, the noise is not only white noise in the *in vivo* measurement. Thus, the influence of the noise variance in the measured spectrum is not always alleviated by elongating the DFT window.

III. Materials and Methods

In this study, the relationship between the maximum detectable velocity and the window length was evaluated by the estimation accuracy of m corresponding to the estimated phase gradient $a'_n(m)$ in (25) (i.e., the stability to the aliasing error). The erroneous estimation of m (i.e., aliasing error), owing to interference between different frequency components, depends on the displacement between frames which is determined by the velocity and the acquisition frame rate. Therefore, the estimation error of the displacement between frames was validated. The single-frequency phased-tracking method [20] or the multifrequency phased-tracking method [26] was applied to the RF signals to estimate the displacement between the frames and the velocity. The detectable maximum displacement was determined from the boundary at which m of the estimated phase gradient $a'_n(m)$ in (25) did not coincide with the true value.

To present an appropriate window function for the rapid motion and the locality of the layered myocardium, Tukey windows were used. The Tukey window $w_T(t)$ is given by

$$w_T(t) = \begin{cases} \frac{1}{2}\left\{1+\cos\left(\frac{2\pi}{r}\left[t-\frac{r}{2}\right]\right)\right\}, & 0 \le t < \frac{r}{2} \\ 1, & \frac{r}{2} \le t < 1-\frac{r}{2} \\ \frac{1}{2}\left\{1+\cos\left(\frac{2\pi}{r}\left[t-1+\frac{r}{2}\right]\right)\right\}, & 1-\frac{r}{2} \le t < 1 \end{cases} \tag{26}$$

where r is the parameter of the Tukey window. Depending on the parameter r, the characteristic of the Tukey window changes between that of the Hanning window ($r = 1$) and the rectangular window ($r = 0$).

A. Confirmation of the Principle

The modeled RF signal in (15) was used to confirm the bias errors in the measured cross-spectrum phases described in Section II-D. The inverse of the standard deviation of the Gaussian function in (15), σ^{-1}, was set to 1.5 MHz. The delay time generated by the displacement between frames was set to 0, 0.067, or 0.20 ms. The cross-spectrum was measured with multiple window lengths. The length of the spatial window changes not only the frequency resolution but also the frequency interval. Thus, zero points were added to the end of the windowed signals in the time domain before applying a DFT. This allowed the original frequency resolution to be maintained [28].

B. Water-Tank Experiments

The influence of the window length of the velocity estimation on the maximum detectable velocity was validated in a water-tank experiment where the true displacement could be measured.

Fig. 5(a) shows a schematic of the water-tank experiment system. A urethane rubber phantom was vibrated up and down sinusoidally at 50 Hz, which was set based on the actual velocity waveform of the heart wall [13], [20]. The maximum velocity was set to approximately 40 mm/s.

The RF signals were acquired using an ultrasonic diagnostic apparatus (Prosound α-10; Hitachi-Aloka-Medical Ltd., Tokyo, Japan) using a sector probe (UST-52101N; Hitachi-Aloka-Medical Ltd., Tokyo, Japan) with a 3.75 MHz center frequency. The transmitted wave was a plane wave without steering and the received beam was formed without compounding. The sampling frequency was set to 15 MHz. As the

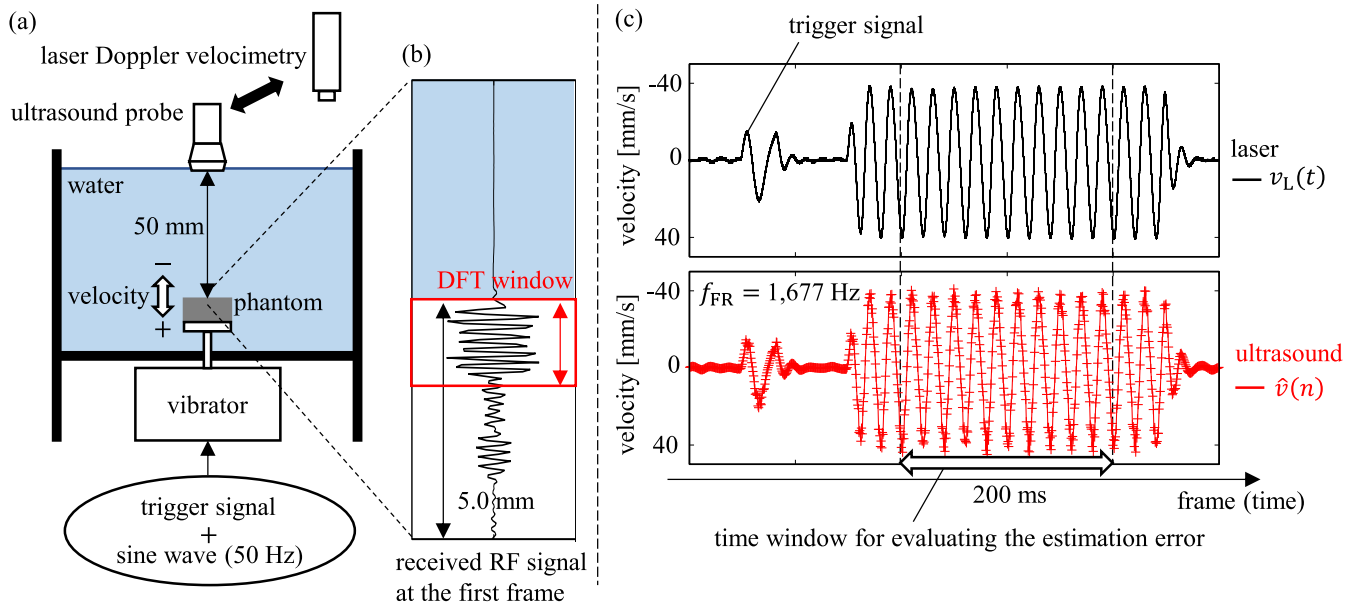

Fig. 5. (a) Schematic of the water tank experiment system. (b) Received RF signal at the first frame. (c) Velocity waveforms measured by laser Doppler velocimetry or ultrasound measurement.

speed of sound in water was 1475 m/s and that in the phantom was 1487 m/s, the RF inter-sample spacing in water was 0.049 mm and that in the phantom was 0.050 mm. The frame rate of the ultrasound measurement was set to 1677 Hz.

The down-sampled frames were used as consecutive frames to estimate the displacement of the phantom. Thus, the velocities of the phantom were estimated at multiple frame rates (1677, 839, 559, ..., and 105 Hz) for the same data. The maximum detectable velocity depends on the frame rate of the ultrasound measurement. Thus, by decreasing the frame rate in the velocity estimation, the displacement between the frames $\Delta z(n)$ became larger than that at the original frame rate. The time interval of the most down-sampled frames at 105 Hz was similar to half the period of the sinusoidal velocity waveform at 50 Hz. Because the phantom moved in the same direction between the most down-sampled frames at 105 Hz, the displacement between these frames had a maximum value of 0.25 mm.

A laser Doppler velocimeter (LV-1300; Ono Sokki, Kanagawa, Japan), which replaced the sector probe, was used for the velocity measurement at the surface of the phantom. The velocity measured by the laser Doppler velocimetry was used as the reference. Fig. 5(c) illustrates the velocity waveforms measured by the laser Doppler velocimetry or the ultrasound measurement and the time window for evaluating the estimation error of the displacement between frames estimated by the ultrasound measurement. As shown in Fig. 5(c), the trigger signals measured by the ultrasound measurement without down-sampling and laser Doppler velocimetry at different timings were synchronized on a computer. The negative effect of the interference between different frequency components depends on the delay time generated by the displacement between frames. Therefore, the reference displacement $\Delta z_R(n)$ was obtained by integrating the velocity measured by the laser Doppler velocimetry, $v_L(t)$, over a time duration corresponding to the frame rate of the ultrasound measurement. The reference displacement $\Delta z_R(n)$ is expressed as follows:

$$\Delta z_R(n) = \int_{n/f_{FR}}^{(n+\Delta n)/f_{FR}} v_L(t)dt. \tag{27}$$

To evaluate the estimation error, the time window was set to ten times the wavelength of the velocity waveforms (200 ms), as shown in Fig. 5(c). The estimation error of the displacement between frames, $e(n)$, was calculated for each pair of frames as

$$e(n) = \left|\widehat{\Delta z}(n) - \Delta z_R(n)\right|. \tag{28}$$

The detectable maximum displacement was determined from the boundary at which there was a large estimation error $e(n)$ caused by the erroneous estimation of m (i.e., aliasing error).

The detectable maximum displacement was also obtained from the simulation described in Section III-A. The inverse of the standard deviation of the Gaussian function in (15), σ^{-1}, was set to 3.0, 1.5, or 1.0 MHz. However, the envelope of the received RF signal in the water-tank experiment differed significantly from a Gaussian function and had the form of a rectangular function, as shown in Fig. 5(b). Considering the actual waveform of the received RF signal, the received RF signal at the first frame in Fig. 5(b) was used as the modeled RF signal at the nth frame $s_m(t; n)$ in (15).

C. Simulation for Determining the Appropriate Window Function for the In Vivo Measurement

For determining the appropriate window function for the rapid motion and the locality of the layered myocardium, the speckle-like waveform in the heart wall and the noise in the actual *in vivo* measurement were simulated.

First, the speckle-like waveform in the heart wall was simulated. Fig. 6(a) shows the schematic of the generation of

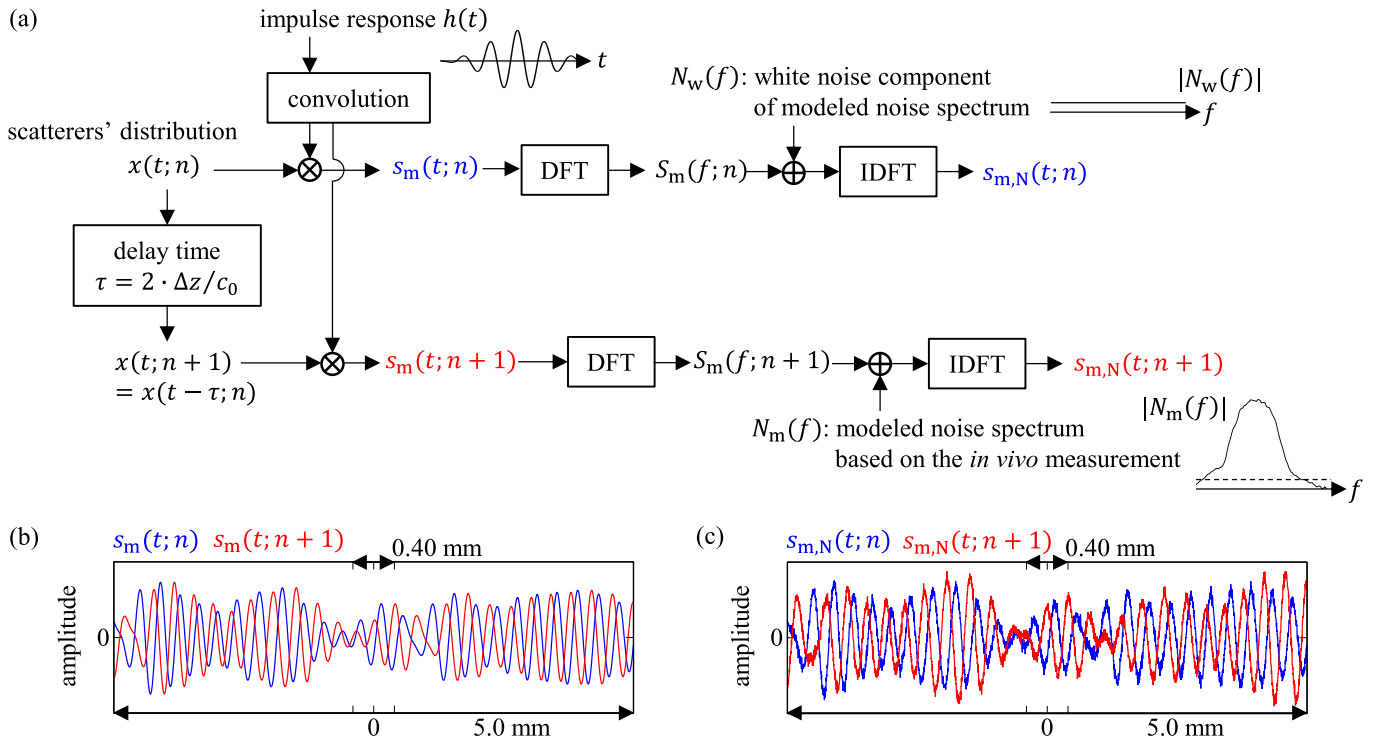

Fig. 6. (a) Schematics of the generation of the modeled RF signal in the simulation. (b) Modeled RF signals without noise, $s_m(t;n)$ and $s_m(t;n+\Delta n)$, in the simulation for the *in vivo* measurement. (c) Modeled RF signals with noise, $s_{m,N}(t;n)$ and $s_{m,N}(t;n+\Delta n)$, in the simulation for the *in vivo* measurement.

the modeled RF signal in the simulation. In this study, the modeled RF signal was based on the convolution model of the impulse response $h(t)$ of the ultrasound transducer in (14) and the scatterers' distribution $x(t;n)$. The inverse of the standard deviation, σ^{-1}, was set to 2.1 MHz relating to the impulse response of the ultrasound transducer that was obtained in measuring a 30 μm-diameter molybdenum wire with a plane wave in a water tank. In simulating the *in vivo* measurement, the multiple scatterers were distributed randomly in the beam direction in space with a density of 15 scatterers per wavelength at the center frequency. The density was based on the diameter of the myocardial fiber and its volume fraction in the heart wall [31]. The scatterers' distribution at the $(n+\Delta n)$th frame was generated by adding an arbitrary delay time $\tau(n)$ to that at the nth frame, which represented the displacement between the nth and the $(n+\Delta n)$th frames. Fig. 6(b) shows the modeled RF signals, $s_m(t;n)$ and $s_m(t;n+\Delta n)$, in the simulation of the *in vivo* measurement when the displacement from the nth frame to the $(n+\Delta n)$th frame was set at 0.14 mm. As shown in Fig. 6(b), the envelopes of the modeled RF signals, $s_m(t;n)$ and $s_m(t;n+\Delta n)$, were similar to the speckle shown in *in vivo* measurements.

Next, the noise in the actual *in vivo* measurement was simulated. In *in vivo* measurements, the change in the waveform of the RF signal occurs due to reasons other than just electronic noise from an ultrasound diagnostic apparatus. This is because the movement in the orthogonal directions to the beam direction and the nonuniform movement around the interest point changes the scatterers' distribution in the heart wall. The change in the waveform between the frames is regarded as a noise in the velocity estimation. Thus, this noise was defined as the different components between the spectra $S(f;n)$ and $S(f;n+\Delta n)$ at the nth and the $(n+\Delta n)$th frames other than the delay time component $e^{-j2\pi\tau(n)f}$ generated by the displacement between the frames.

The noise spectrum $N(f;n)$ can be obtained by subtracting the product of the spectrum at the nth frame $S(f;n)$ and the delay time component $e^{-j2\pi\tau(n)f}$ from the spectrum at the $(n+\Delta n)$th frame $S(f;n+\Delta n)$. However, the true delay time $\tau(n)$ cannot be known or measured in the *in vivo* measurement. In this study, the estimated delay time $\hat{\tau}(n)$ using a long DFT window ($L_{DFT} = 10$ mm) was used to obtain the noise spectrum. Because the long DFT window has a high-frequency resolution, the spectra $S(f;n)$ and $S(f;n+\Delta n)$, and the delay time component $e^{-j2\pi\tau(n)f}$ can be estimated without the interference between the different frequency components. The noise spectrum $N(f_k;n)$ and the signal-to-noise ratio (SNR) $\rho(n)$ in the velocity estimation were defined as

$$N(f_k;n) = S(f_k;n+\Delta n) - S(f_k;n)\cdot e^{-j2\pi\hat{\tau}(n)\cdot f_k} \quad (29)$$

$$\rho(n) = 10\log_{10}\frac{\sum_{f_k=0}^{f_s/2} S(f_k;n)^2}{\sum_{f_k=0}^{f_s/2} N(f_k;n)^2} \quad (30)$$

where $S(f_k;n)$ and $S(f_k;n+\Delta n)$ are the measured spectra at the nth and the $(n+\Delta n)$th frames, respectively. Therefore, a sophisticated simulation can be realized using the noise spectrum $N(f_k;n)$ based on the *in vivo* measurement.

In this study, the noise spectrum was modeled based on the *in vivo* measurement to evaluate the average performance in the velocity estimation in the heart wall. The noise spectrum

$N(f_k; n)$ was obtained from the measurements of the interventricular septum (IVS) in the parasternal long-axis view during a cardiac cycle, which will be explained in detail in Section III-D. Because the bandwidth of the noise spectrum was almost the same during a cardiac cycle, its amplitude was generalized by the average over the cardiac cycle and was used as that of the modeled noise spectrum $|N_m(f; n)|$ in the simulation. The phase of the noise spectrum $\angle N(f_k; n)$ was different between adjacent frequency components and between the consecutive frames. Because the noise spectrum phase was uniformly random in both the frequency domain and the cardiac cycle, in this study, it was assumed that the phase of the noise spectrum was uniformly random. The phase of the modeled noise spectrum $\angle N_m(f; n)$ was generalized as a random value corresponding to the uniform distribution. Considering the velocity-estimation SNR obtained in the *in vivo* measurement, we added the modeled noise spectrum $N_m(f; n)$ to the spectrum of the modeled RF signal at the $(n + \Delta n)$th frame, $S_m(f; n + \Delta n)$, as shown in Fig. 6(a). The modeled RF signal at the nth frame may be affected by the electronic noise from an ultrasound diagnostic apparatus with the same power as that at the $(n + \Delta n)$th frame. Because the electronic noise is often regarded as white noise, the white noise component $N_W(f; n)$ included in the modeled noise spectrum was added to the spectrum of the modeled RF signal at the nth frame, $S_m(f; n)$. The power of the white noise component was almost a tenth of that of the modeled noise spectrum. Fig. 6(c) shows the modeled RF signals with noise, $s_{m,N}(t; n)$ and $s_{m,N}(t; n + \Delta n)$, these are obtained by adding the noise spectrum $N_m(f; n)$ with the velocity-estimation SNR of 7 dB to the modeled RF signals without noise in Fig. 6(b). As shown in Fig. 6(c), the envelope of the modeled RF signals with noise at the $(n + \Delta n)$th frame, $s_{m,N}(t; n + \Delta n)$, was different from that at the nth frame, $s_{m,N}(t; n)$. This cannot be expressed by adding only the white noise to the modeled RF signal.

The relationship between the maximum detectable displacement and the window length was obtained using the modeled RF signals with noise, $s_{m,N}(t; n)$ and $s_{m,N}(t; n+\Delta n)$. However, the detectable maximum displacement based on the estimation accuracy of m (i.e., the stability to the aliasing error) is not uniquely determined because the scatterers' distribution was random and the noise caused the variance in the cross-spectrum phase. Thus, the probability of an aliasing error was calculated for 100 generations of $s_{m,N}(t; n)$ and $s_{m,N}(t; n + \Delta n)$ for each displacement and window length. The maximum detectable displacement was evaluated using the calculated probability of the aliasing error.

In addition, the performance of the window function was evaluated on the window length that can measure the maximum displacement between frames in the heart wall with the permitted value of the probability of the aliasing error. In this study, the permitted value of the probability of the aliasing error was set to 0.05 or 0.10. Furthermore, in this study, the maximum velocity in the transmural direction of the heart wall was obtained using the long DFT window ($L_{DFT} = 10$ mm) similar to the noise spectrum and the SNR in the velocity estimation. The appropriate window function and window length for the local velocity estimation was determined based on the result of the simulation.

D. In Vivo Experiments

In the *in vivo* experiment, the improvement of the maximum detectable velocity by using the multifrequency phase differences was validated and the performance of the window function in improving the maximum detectable velocity was compared.

In vivo measurements were applied to the IVS of a healthy 23-year-old subject. The study was approved by the Ethics Committee of Graduate School of Engineering, Tohoku University, Sendai, Japan, and the subject agreed to participate in this study. The RF signal was acquired using an ultrasonic diagnostic apparatus (Prosound α-10; Hitachi-Aloka-Medical Ltd., Tokyo, Japan) with a sector probe (UST-52101N; Hitachi-Aloka-Medical Ltd., Tokyo, Japan) having a 3.75 MHz center frequency. The seven plane waves in seven different directions at the steering angles of 6° intervals were transmitted and compounded to obtain each received beam [32]. The sampling frequency was set to 15 MHz. Since the speed of sound in living tissue was assumed to be 1540 m/s, the RF inter-sample spacing in the tissue was estimated as 0.051 mm. The frame rate of the ultrasound measurement was set at 860 Hz. The electrocardiogram (ECG) was acquired using the three-point lead method, and the ECG waveform was obtained from lead II. The phonocardiogram (PCG) waveform was measured using a small accelerometer attached to the subject's chest.

The improvement of the maximum detectable velocity by using the multifrequency phase differences was validated by comparing the velocity waveform estimated locally by the single-frequency or multifrequency phased-tracking method. The interest point of the velocity estimation was tracked in the beam direction by integrating the estimated velocity waveform. The performances of the window functions in improving the maximum detectable velocity were compared by estimating the velocities by applying different window functions with the same length.

IV. Results

A. Bias Errors in the Measured Cross-Spectrum Phases

Fig. 7 shows the measured cross-spectrum between the modeled RF signals without noise obtained using multiple window lengths when a single point scatterer was set on the ultrasound beam. The color bar shows the length of the DFT window. Fig. 7(a)–(c) shows the cross-spectrum at delay times of 0, 0.067, and 0.20 ms, respectively.

In Fig. 7(a), where the delay time was set at 0 ms, the measured phase corresponded to the true phase at all discrete frequencies. This was because both the true cross-spectrum in (17) and the measured cross-spectrum in (23), in which 0 ms was substituted for $\tau(n)$, had a zero-phase characteristic even when the frequency resolution was poor (red points). Thus, the influence of the interference between different frequency components was small when the delay time was small.

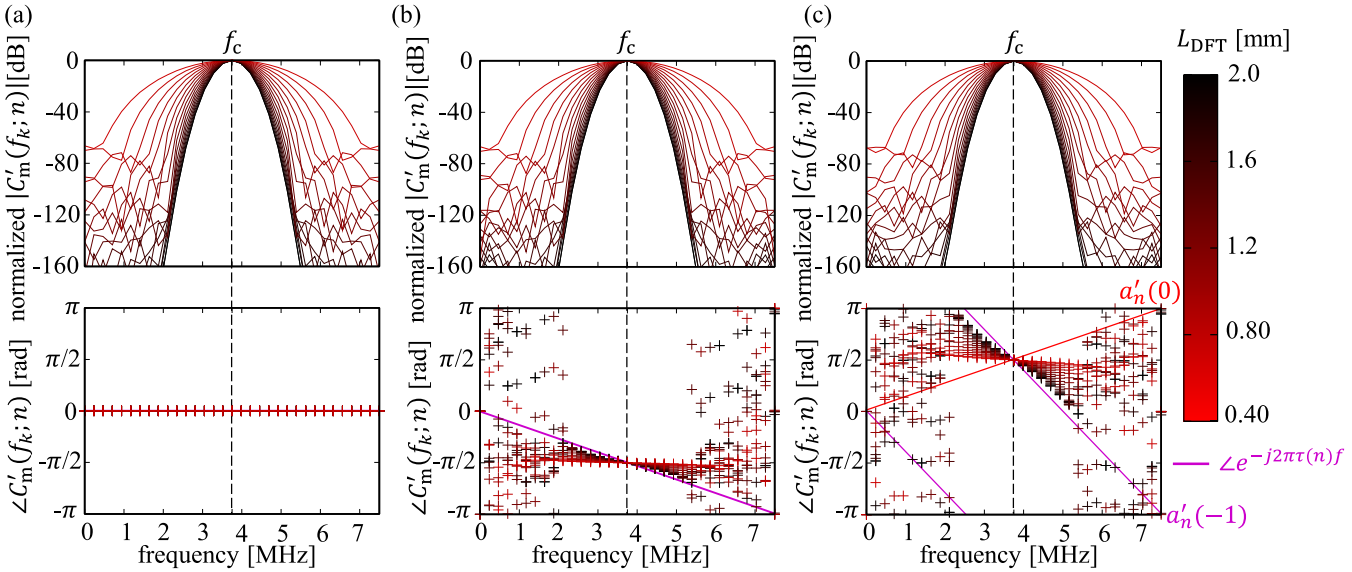

Fig. 7. Measured cross-spectrum $C'_m(f_k; n)$ obtained using multiple window lengths. The cross-spectrum with delay times set at (a) 0, (b) 0.067, and (c) 0.20 ms.

In Fig. 7(b), the true phase gradient was given by $a'_n(0)$ in (25) because the delay time (0.067 ms) did not exceed half the period of the center frequency. The bias errors became large and the apparent phase gradient decreased with the decrease in frequency resolution (red points). However, the true phase gradient could be estimated because the true value of m was minimal and the noise component was not added to the modeled RF signal. Thus, the erroneous estimation of m in the possible phase gradient did not occur when the phase of the cross-spectrum did not wrap and there was no additional noise.

In Fig. 7(c), the true phase gradient was given by $a'_n(-1)$ in (25) because the phase of the cross-spectrum was wrapped once from a negative value to a positive value. The bias errors increased as the frequency resolution decreased (red points) and as the apparent phase gradient decreased. These bias errors caused the erroneous estimation of m in the possible phase gradient $a'_n(m)$ in (25). Thus, the phase gradient was estimated not as $a'_n(-1)$ (purple solid line), but as $a'_n(0)$ (red solid line) when the frequency resolution was poor (red points). This erroneous estimation resulted in a large displacement error. Thus, in Fig. 7(c), the influence of the interference between different frequency components on the velocity estimation could not be suppressed despite the use of the cross-spectrum amplitude as the weighting function.

B. Water-Tank Experiment

Fig. 8 shows the spectra of the window function and the estimation errors in the single-frequency and multifrequency phased-tracking methods in the water-tank experiment. In Fig. 8(b)–(d), the horizontal axis represents the length of the window function and the vertical axis represents the reference displacement between frames, Δz_R. The color bar shows the estimation error of the displacement between frames, $e(n)$. The blue points represent a small estimation error, and the red points represent a large estimation error. The red dashed line shows the maximum detectable displacement in the single-frequency phased-tracking method, $|\widehat{\Delta z}_{f_c,\mathrm{MAX}}|$. The green solid line shows the maximum displacement $|\widehat{\Delta z}_{\mathrm{MAX}}|$ limited by the frequency interval.

As shown in Fig. 8(b), a large displacement error occurred because of aliasing when the displacement of the phantom exceeded the maximum detectable displacement between frames ($|\widehat{\Delta z}_{f_c,\mathrm{MAX}}| < \Delta z_R$). The boundary between the small displacement errors (blue points) and the large displacement errors (red points) is considered to be the maximum detectable displacement because the erroneous estimation of m occurred there. The maximum detectable displacement in the single-frequency phased-tracking method did not depend on the length of the window function as is evident from (5).

As shown in Fig. 8(c) and (d), the estimation errors in the multifrequency phased-tracking method depend on the length of the window function. The maximum detectable displacement was increased by the use of multifrequency phase differences, but it decreased as the length of the window was decreased. This is consistent with the simulation results (black solid line). The maximum detectable displacement was smaller than the maximum displacement limited by the frequency interval $|\widehat{\Delta z}_{\mathrm{MAX}}|$ in both the simulations and the water-tank experiment. This is because the poor frequency resolution made it difficult to measure large displacements.

The relationship between the maximum detectable displacement and the window length obtained in the water-tank experiment did not correspond to those in the simulation using the impulse response in (14), which had an envelope similar to a Gaussian function. This was observed even though it was confirmed that the maximum detectable displacement decreased as the length of the window was decreased in both the simulation and the water-tank experiment. In Fig. 8(c) and (d), the purple solid lines show the maximum detectable displacement obtained in the simulation using the received RF signal from the water-tank experiment. This result corresponded well with the maximum detectable displacement

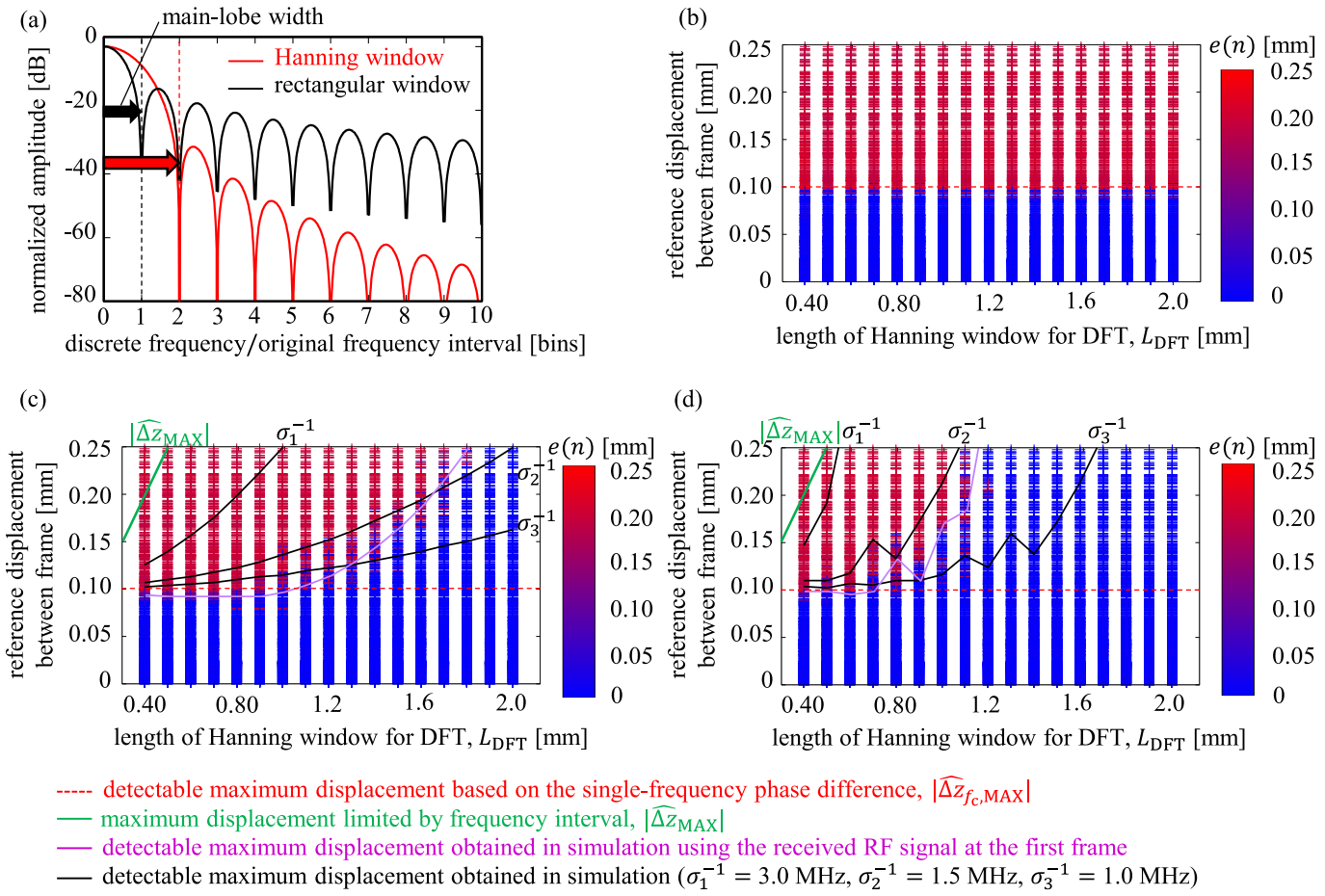

Fig. 8. (a) Spectrum of window function, (b) estimation error of the displacement between frames in the single-frequency phased-tracking method with a Hanning window, (c) that in the multifrequency phased-tracking method with a Hanning window, and (d) that in the multifrequency phased-tracking method with a rectangular window.

obtained in the water-tank experiment, that is, the relationship between the maximum detectable displacement and the locality of the velocity estimation also depended on the waveform of the received RF signal.

The relationships between the maximum detectable displacement and the length of the DFT window differed according to the window function. As shown in Fig. 8(d), a larger maximum detectable displacement can be obtained using a rectangular window than by using a Hanning window. Because the mainlobe width of the rectangular window is half that of the Hanning window, as shown in Fig. 8(a), the frequency resolution of the former is twice that of the latter. Thus, the maximum detectable displacement of the rectangular window approximately corresponded to that of the Hanning window with twice the length of the spatial window.

As shown in Fig. 8(d), the maximum detectable displacement of the rectangular window did not monotonically increase with the increase in the window length in both the simulations and the water-tank experiment. This might be due to the spectral leakage caused by the discontinuity at both edges of the rectangular window. The spectral leakage is caused by the discontinuity at both edges of the window [33]. When the window length is not an integer multiple of the wavelength, there is a discontinuity in the phase of the signal between the edges of the window, and the spectral leakage increases. In addition, the delay time of the signal causes a discontinuity in the amplitude of the signal at both edges of the window and increases the spectral leakage because the envelope amplitude of the modeled RF signal is not constant. The spectral leakage caused by the discontinuity at both edges negatively affected the maximum detectable displacement and resulted in the non-monotonic relationship between the maximum detectable displacement and the length of the rectangular window. By contrast, the Hanning window is a window with a low sidelobe level [34]. Thus, the relationship between the maximum detectable displacement and the length of the Hanning window depended mainly on the frequency resolution and its maximum detectable displacement monotonically increased with the increase in the window length, as shown in Fig. 8(c).

C. Determining the Appropriate Window Function for the In Vivo Measurement

In vivo measurement, the maximum velocity estimated using the long DFT window of 10 mm was 116 mm/s. Thus, we predicted that the maximum displacement that should be measured in the simulation, $|\widehat{\Delta z}_{\mathrm{MAX}}|$, was 0.14 mm. In simulating the *in vivo* measurement, the SNR in the velocity

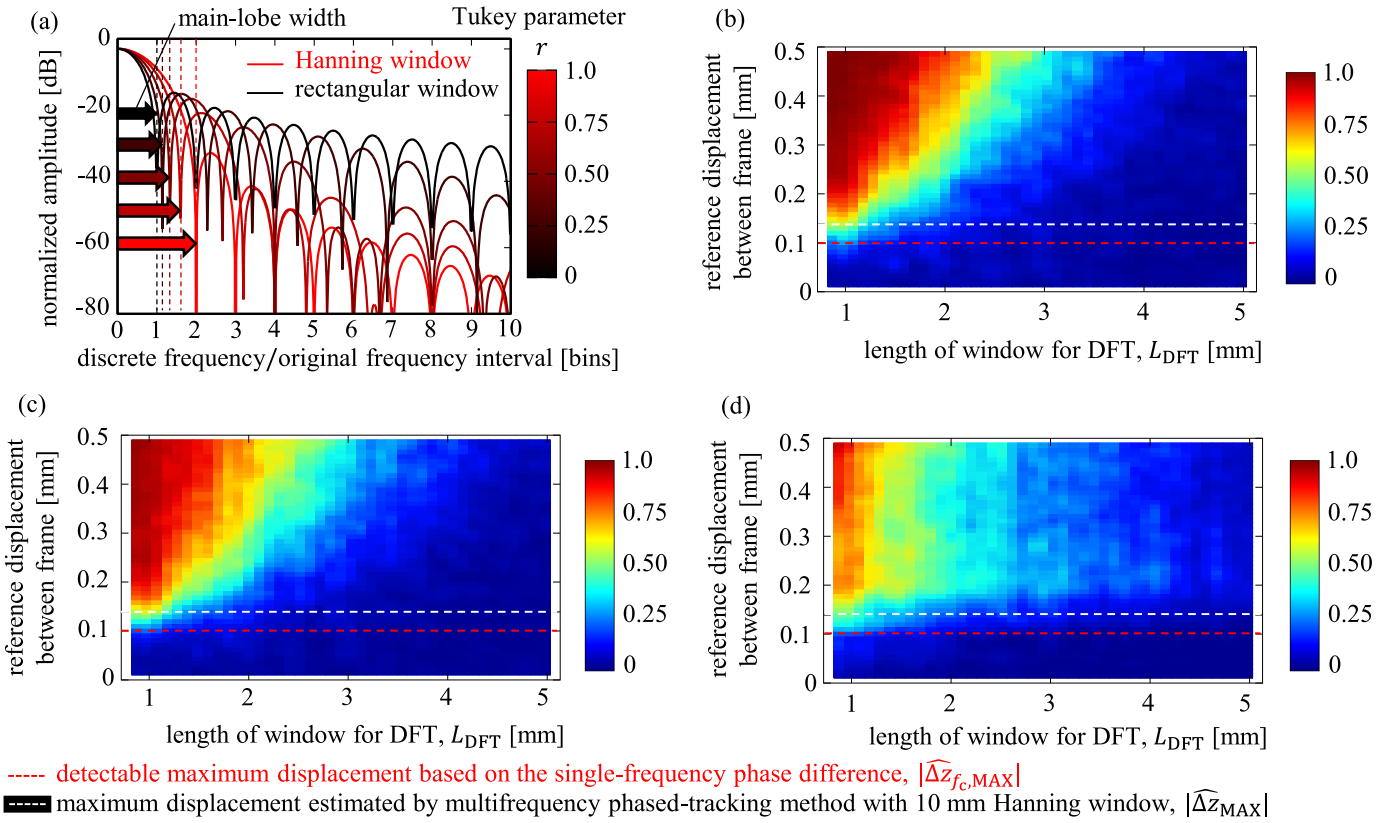

Fig. 9. (a) Spectrum of the Tukey window, probability of an aliasing error in the multifrequency phased-tracking method with the Tukey window where the parameter (b) $r = 1$, (c) $r = 0.50$, and (d) $r = 0$.

estimation was set to 7 dB, which was obtained as in (30) using the long DFT window at the time when the velocity in the heart wall was larger than the maximum detectable velocity based on a single-frequency phase difference.

Fig. 9 shows the spectra of the window functions and the probability of an aliasing error in the multifrequency phased-tracking method in the simulation of the *in vivo* measurement. In Fig. 9(b)–(d) the horizontal axis represents the length of the window function and the vertical axis represents the true displacement between frames, Δz. The color bar shows the probability of an aliasing error in the multifrequency phased-tracking method. The blue area represents a stable estimation. The red area represents an unstable estimation owing to the aliasing error. The red dashed line shows the maximum detectable displacement in the single-frequency phased-tracking method, $|\widehat{\Delta z}_{f_c,\mathrm{MAX}}|$.

As shown in Fig. 9(b) and (d), the area where the probability of an aliasing error was high (red area) in the result using the Hanning window was broader than that in the result using the rectangular window. This might be representative of the difference in the frequency resolution depending on the mainlobe width, which corresponded to the result of the water-tank experiment in Fig. 8. However, as shown in Fig. 9(d), it was not easy to decrease the probability of an aliasing error when using the rectangular window even though the window length was increased. This may be a negative effect of the discontinuity at both edges of the windowed signal. This negative effect was not ameliorated by elongating the DFT window and could not be ignored in simulating the *in vivo* measurement.

As shown in Fig. 9(c), this negative effect was ameliorated in the result using the Tukey window ($r = 0.50$). Because the Tukey window ($r = 0.50$) has a higher frequency resolution than the Hanning window as shown in Fig. 9(a), the maximum detectable displacement of the Tukey window ($r = 0.50$) may be larger than that of the Hanning window. There is a tradeoff between the frequency resolution and the negative effect of the discontinuity at both edges of the windowed signal. Depending on the parameter r in (26), the characteristic of the Tukey window changes between that of the Hanning window and the rectangular window, as shown in Fig. 9(a). Thus, the Tukey window is useful to optimize this tradeoff. The performance of the Tukey window was evaluated for each value of parameter r in (26).

Fig. 10 shows the minimum value of the window length that can measure the maximum displacement between frames in the heart wall (0.14 mm) with the permitted value of the probability of an aliasing error. In Fig. 10, the permitted value of the probability of the aliasing error was set to 0.05 (black line) or 0.10 (blue line). As shown in Fig. 10, the Tukey window ($r = 0.30$) shows the best performance to locally measure the maximum displacement of 0.14 mm in both the permitted values of the probability of the aliasing error. When the permitted value of the probability of the aliasing error was set to 0.05, the shortest Tukey window ($r = 0.30$) was 2.5 mm. In this window function, the length of the tapered part toward

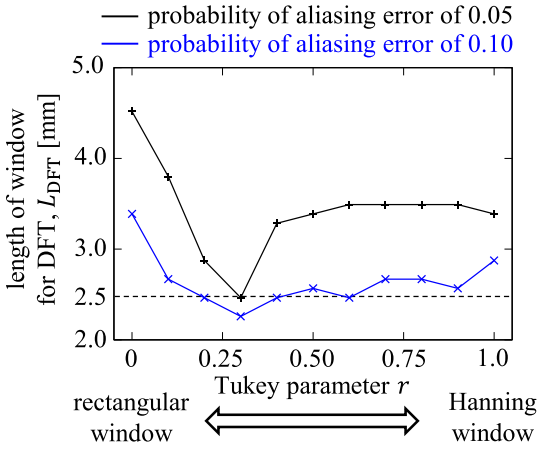

Fig. 10. Minimum value of the Tukey window length that can measure the maximum displacement between frames in the heart wall with the permitted value of the probability of an aliasing error.

the edge approximately corresponded to two wavelengths (0.40 mm) at each edge. This might ameliorate the negative effect of the discontinuity at both edges of the windowed signal in the rectangular window.

Interestingly, the Hanning window, which has a low sidelobe level, was inferior to the Tukey window ($r = 0.30$) even when the noise was present. As shown in Fig. 6(a), the power of the white noise component was almost a tenth of that of the modeled noise spectrum $N_{\mathrm{m}}(f; n)$. Thus, the advantage of the low sidelobe level of the Hanning window might not be effective. The Tukey window ($r = 0.30$) has a high-frequency resolution and ameliorates the negative effect of the discontinuity at both edges because the Tukey window ($r = 0.30$) has a flat part around the center and the tapered part toward the edges, as in (26). Thus, the Tukey window ($r = 0.30$) shows a better performance in improving the maximum detectable displacement than the Hanning window.

D. In Vivo Experiment Using the Appropriate Window Function Determined in the Simulation

In the result of the simulation considering the *in vivo* measurement condition, the appropriate window function was the Tukey window ($r = 0.30$), as shown in Fig. 10. In the *in vivo* experiment, the performance of the Tukey window ($r = 0.30$) in improving the maximum detectable velocity was compared with that of the Hanning window, which was used in our previous studies [18], [26], [27]. Fig. 11 shows the B-mode image of the IVS from the parasternal long-axis view, the ECG waveform, the PCG waveform, and the velocity waveforms estimated using the single-frequency and multifrequency phased-tracking methods. In Fig. 11(a), the yellow dot represents the interest point of the velocity estimation where the center of the window function was set. In Fig. 11(d) and (e), the red dashed line represents the detectable maximum velocity based on the single-frequency phase difference, $|\hat{v}_{f_c,\mathrm{MAX}}|$.

As shown in Fig. 11(d), around the time from the ECG R-wave of 30 and 640 ms, aliasing errors occurred in the velocity waveform estimated using the single-frequency phased-tracking method with the 2.5 mm Hanning window (red line) or the 2.5 mm Tukey window ($r = 0.30$) (blue line). In the single-frequency phased-tracking method, there was no significant difference in the number of aliasing errors between the velocity waveforms estimated with the Hanning window and the Tukey window ($r = 0.30$). This was because the maximum detectable displacement in the single-frequency phased-tracking method does not depend on the frequency resolution, as confirmed in the water-tank experiment.

As shown in Fig. 11(e), the number of aliasing errors in the velocity waveforms decreased using the multifrequency phased-tracking method. Thus, the maximum detectable velocity was improved by the use of the multifrequency phase differences. However, in the result of the Hanning window [red line in Fig. 11(e)], aliasing errors were not completely suppressed, and they also occurred around the time from the ECG R-wave at 400 ms even though the velocity waveform was estimated using the multifrequency phase differences. In this case, the length of the Hanning window should be increased to suppress the aliasing errors. By contrast, in the result of the Tukey window ($r = 0.30$) [blue line in Fig. 11(e)], an aliasing error did not occur during a cardiac cycle due to the advantage of a high-frequency resolution. In addition, at the time from the ECG R-wave of 30 ms, when the estimated velocity using the long DFT window of 10 mm was maximum, the velocities at all the spatial points in the IVS (13674 points) were estimated using the multifrequency phased-tracking method with the Hanning window or the Tukey window ($r = 0.30$). The number of points where an aliasing error occurred is 608 (4%) or 302 (2%) in using the Hanning window or the Tukey window ($r = 0.30$), respectively. These results suggested that the Tukey window ($r = 0.30$) was useful for improving the maximum detectable velocity in the *in vivo* measurement while maintaining the locality of the velocity estimation.

V. Discussion

The maximum detectable velocity was improved by using the multifrequency phase difference in both the water-tank experiment and the *in vivo* experiment. Even though this maximum detectable velocity was negatively affected by the interference between the different frequency components, it was larger than the maximum detectable velocity based on a single-frequency phase difference when the cross-spectrum amplitude was used as the weighting function. Thus, the multifrequency velocity estimator was useful for measuring the rapid motion of the heart wall.

In this study, the plane wave was transmitted from the sector probe. Diverging waves were used to measure the large field of view, and the measurement using diverging waves was proposed for the strain measurement of the heart wall [32], [35], [36]. There is no significant difference in the spatial resolution in the beam direction between the plane wave and the diverging wave [32], [37]. Thus, the condition of the transmitted wave may not affect the relationship between the maximum detectable displacement and the window length. However, the SNR in the velocity estimation may depend

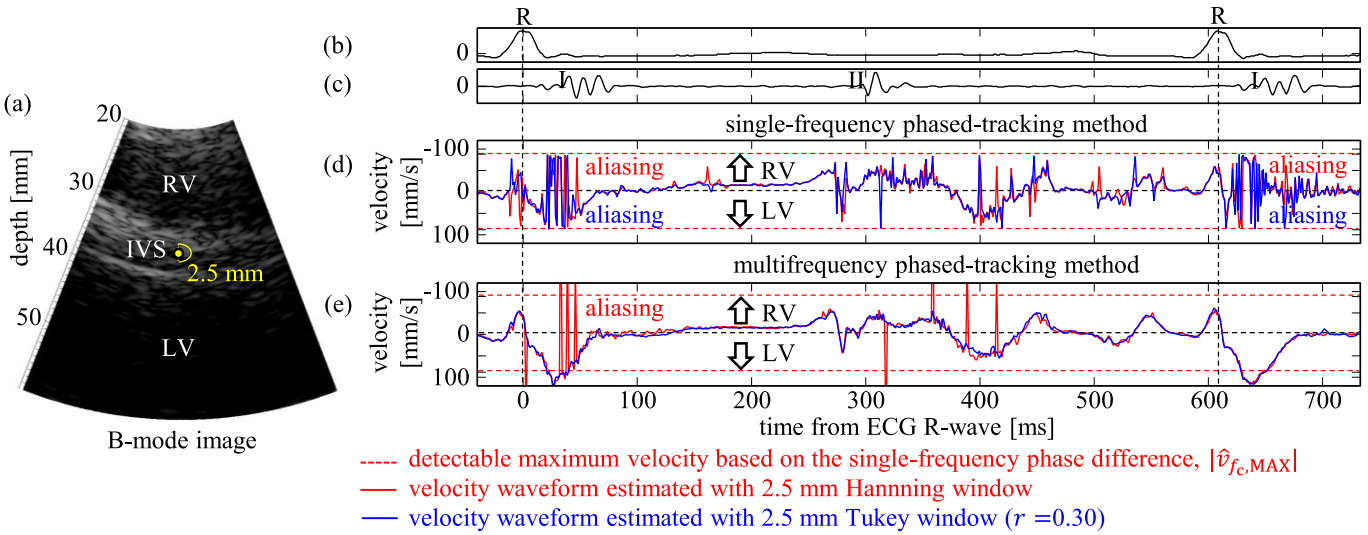

Fig. 11. (a) B-mode image of the IVS of a healthy young subject in measurement from the parasternal long-axis view. (b) ECG waveform, (c) PCG waveform, and (d) velocity waveform estimated using a single-frequency phased-tracking method with a 2.5 mm Hanning window or a 2.5 mm Tukey window ($r = 0.30$). (e) Velocity waveform estimated using a multifrequency phased-tracking method with a 2.5 mm Hanning window or a 2.5 mm Tukey window ($r = 0.30$). (LV: left ventricular, RV: right ventricular).

on the transmitted wave condition owing to the difference in the temporal resolution and the spatial resolution in the orthogonal direction to the beam direction. Because the noise in the velocity estimation is related to the movement of the heart wall, as described in Section III-C, the changes in the temporal resolution and the spatial resolution in the orthogonal directions may affect the power of the noise spectrum. Even though the transmitted wave was not a plane wave, the SNR in the velocity estimation can be validated by the present method. Therefore, the methods of this study may be beneficial for the SR measurement using diverging waves.

Let us discuss the determination of the appropriate window length based on the relationship between the maximum detectable velocity and the window length for the local SR measurement in the heart wall. In this study, the *in vivo* experiment was applied to the IVS from the parasternal long-axis view and the velocity in the transmural direction was measured. The multifrequency phased-tracking method estimated only the velocity in the beam direction. Thus, the heart wall was measured from the parasternal long-axis view, short-axis view, or the apical view depending on the velocity component that we want to measure. The maximum velocity in the heart wall can be approximately predicted based on the reference value for each measurement view, region of the heart wall, and cardiac periods. The reference value is measurable by the multifrequency phased-tracking method with a long DFT window, which can detect a sufficiently high displacement, as described in Section III-C. The maximum velocity in the longitudinal direction is larger than that in the transmural direction [38], [39]; the appropriate window length for estimating the longitudinal component may be longer than that for estimating the transmural one.

The 1-D strain and SR imaging method have been used for clinical applications [7], [40]–[42], and the 2-D or 3-D strain and SR imaging have also been studied [43]–[45]. The multifrequency phased-tracking method can be expanded to the 2-D or 3-D velocity estimator if needed [46], [47]. In the beam direction of the 2-D or 3-D velocity estimator based on the multifrequency phase differences, the relationship between the maximum detectable velocity and the window length may correspond to that in this study.

The computational cost in using the multifrequency phase differences increases as the number of the analysis discrete frequencies used for estimating the cross-spectrum phase gradient increases. Thus, the computational cost of the velocity estimator based on the multifrequency phase differences is higher than that based on a single-frequency phase difference. One of the methods to decrease the computational cost is to impose a limitation on the frequency components used for estimating the cross-spectrum phase gradient. It is our future work to implement the multifrequency phased-tracking method to an ultrasound diagnostic apparatus for real-time imaging.

VI. Conclusion

In this article, the relationship between the maximum detectable velocity and the window length in the velocity estimation based on the multifrequency phase differences was described theoretically. The interference between different frequency components in a short DFT window causes bias errors in the phase differences at discrete frequencies other than the center frequency. This decreased the maximum detectable velocity and caused a large estimation error in the velocity. The tradeoff between the maximum detectable velocity and the window length was confirmed through simulations and a water-tank experiment. Under the tradeoff, the Hanning window, which was used in previous studies, is not always appropriate for the local measurement of the velocity, which sometimes exceeds 100 mm/s depending on the subject, direction of the ultrasound beam to the heart wall, and cardiac periods. In the *in vivo* measurement with the short window, the Tukey window with a large flat part, which has a high-frequency resolution and ameliorates the discontinuity at both

edges of the windowed signal, was appropriate for measuring the maximum velocity of the heart wall. This study offers the potential for the local velocity and SR measurements of each myocardial layer using the multifrequency velocity estimator with the appropriate window function and window length.

REFERENCES

[1] K. J. Foreman *et al.*, "Forecasting life expectancy, years of life lost, and all-cause and cause-specific mortality for 250 causes of death: Reference and alternative scenarios for 2016–40 for 195 countries and territories," *Lancet*, vol. 392, no. 10159, pp. 2052–2090, Nov. 2018, doi: 10.1016/S0140-6736(18)31694-5.

[2] K. A. Reimer, J. E. Lowe, M. M. Rasmussen, and R. B. Jennings, "The wavefront phenomenon of ischemic cell death. 1. myocardial infarct size vs duration of coronary occlusion in dogs," *Circulation*, vol. 56, no. 5, pp. 786–794, Nov. 1977, doi: 10.1161/01.CIR.56.5.786.

[3] H. Fujiwara, M. Ashraf, S. Sato, and R. W. Millard, "Transmural cellular damage and blood flow distribution in early ischemia in pig hearts," *Circulat. Res.*, vol. 51, no. 6, pp. 683–693, Dec. 1982, doi: 10.1161/01.RES.51.6.683.

[4] H. Kanaide, Y. Taira, and M. Nakamura, "Transmural anoxic wave front and regional dysfunction during early ischemia," *Amer. J. Physiol.-Heart Circulatory Physiol.*, vol. 253, no. 2, pp. H240–H247, Aug. 1987, doi: 10.1152/ajpheart.1987.253.2.H240.

[5] H. Kanai, H. Hasegawa, N. Chubachi, Y. Koiwa, and M. Tanaka, "Noninvasive evaluation of local myocardial thickening and its color-coded imaging," *IEEE Trans. Ultrason., Ferroelectr., Freq. Control*, vol. 44, no. 4, pp. 752–768, Jul. 1997, doi: 10.1109/58.655190.

[6] A. Heimdal, A. Støylen, H. Torp, and T. Skjærpe, "Real-time strain rate imaging of the left ventricle by ultrasound," *J. Amer. Soc. Echocardiography*, vol. 11, no. 11, pp. 1013–1019, Nov. 1998, doi: 10.1016/S0894-7317(98)70151-8.

[7] J. D'hooge *et al.*, "Regional strain and strain rate measurements by cardiac ultrasound: Principles, implementation and limitations," *Eur. Heart J.-Cardiovascular Imag.*, vol. 1, no. 3, pp. 154–170, Sep. 2000, doi: 10.1053/euje.2000.0031.

[8] R. B. Shenouda, I. Bytyçi, M. Sobhy, and M. Y. Henein, "Reduced regional strain rate is the most accurate dysfunction in predicting culprit lesions in patients with acute coronary syndrome," *Clin. Physiol. Funct. Imag.*, vol. 40, no. 1, pp. 21–29, Jan. 2020, doi: 10.1111/cpf.12597.

[9] C. Pislaru, M. Belohlavek, R. Y. Bae, T. P. Abraham, J. F. Greenleaf, and J. B. Seward, "Regional asynchrony during acute myocardial ischemia quantified by ultrasound strain rate imaging," *J. Amer. College Cardiol.*, vol. 37, no. 4, pp. 1141–1148, Mar. 2001.

[10] M. Belohlavek, C. Pislaru, R. Y. Bae, J. F. Greenleaf, and J. B. Seward, "Real-time strain rate echocardiographic imaging: Temporal and spatial analysis of postsystolic compression in acutely ischemic myocardium," *J. Amer. Soc. Echocardiography*, vol. 14, no. 5, pp. 360–369, May 2001, doi: 10.1067/mje.2001.110786.

[11] C. Pislaru, P. C. Anagnostopoulos, J. B. Seward, J. F. Greenleaf, and M. Belohlavek, "Higher myocardial strain rates during isovolumic relaxation phase than during ejection characterize acutely ischemic myocardium," *J. Amer. College Cardiol.*, vol. 40, no. 8, pp. 1487–1494, Oct. 2002.

[12] F. Jamal *et al.*, "Can changes in systolic longitudinal deformation quantify regional myocardial function after an acute infarction? An ultrasonic strain rate and strain study," *J. Amer. Soc. Echocardiography*, vol. 15, no. 7, pp. 723–730, Jul. 2002, doi: 10.1067/mje.2002.118913.

[13] H. Kanai, "Propagation of vibration caused by electrical excitation in the normal human heart," *Ultrasound Med. Biol.*, vol. 35, no. 6, pp. 936–948, Jun. 2009, doi: 10.1016/j.ultrasmedbio.2008.12.013.

[14] A. Hayashi, S. Mori, M. Arakawa, and H. Kanai, "Local two-dimensional distribution of propagation speed of myocardial contraction for ultrasonic visualization of contraction propagation," *Jpn. J. Appl. Phys.*, vol. 58, no. SG, Jun. 2019, Art. no. SGGE05, doi: 10.7567/1347-4065/ab0d0b.

[15] H. Kanai, S. Mori, and M. Arakawa, "Speeds of contraction responses propagating along septum at pre-ejection period are different between radial and longitudinal directions," in *Proc. IEEE Int. Ultrason. Symp. (IUS)*, Oct. 2019, pp. 1418–1420, doi: 10.1109/ULTSYM.2019.8925990.

[16] H. Yoshiara, H. Hasegawa, H. Kanai, and M. Tanaka, "Ultrasonic imaging of propagation of contraction and relaxation in the heart walls at high temporal resolution," *Jpn. J. Appl. Phys.*, vol. 46, no. 7B, pp. 4889–4896, Jul. 2007, doi: 10.1143/JJAP.46.4889.

[17] M. Tanaka *et al.*, "A new concept of the contraction–extension property of the left ventricular myocardium," *J. Cardiol.*, vol. 63, no. 4, pp. 313–319, Apr. 2014, doi: 10.1016/j.jjcc.2013.09.009.

[18] Y. Obara, S. Mori, M. Arakawa, and H. Kanai, "Measurement of propagation of local and minute contractile response in layered myocardium," *Jpn. J. Appl. Phys.*, vol. 60, Mar. 2021, Art. no. SDDE02, doi: 10.35848/1347-4065/abeabf.

[19] W. N. McDicken, G. R. Sutherland, C. M. Moran, and L. N. Gordon, "Color Doppler velocity imaging of the myocardium," *Ultrasound Med. Biol.*, vol. 18, nos. 6–7, pp. 651–654, 1992, doi: 10.1016/0301-5629(92)90080-T.

[20] H. Kanai, M. Sato, Y. Koiwa, and N. Chubachi, "Transcutaneous measurement and spectrum analysis of heart wall vibrations," *IEEE Trans. Ultrason., Ferroelectr., Freq. Control*, vol. 43, no. 5, pp. 791–810, Sep. 1996, doi: 10.1109/58.535480.

[21] C. Jia *et al.*, "Comparison of 2-D speckle tracking and tissue Doppler imaging in an isolated rabbit heart model," *IEEE Trans. Ultrason., Ferroelectr., Freq. Control*, vol. 57, no. 11, pp. 2491–2502, Nov. 2010, doi: 10.1109/TUFFC.2010.1715.

[22] H. Kanai, Y. Koiwa, and J. Zhang, "Real-time measurements of local myocardium motion and arterial wall thickening," *IEEE Trans. Ultrason., Ferroelectr., Freq. Control*, vol. 46, no. 5, pp. 1229–1241, Sep. 1999, doi: 10.1109/58.796128.

[23] H. J. Nitzpon, J. C. Rajaonah, C. B. Burckhardt, B. Dousse, and J.-J. Meister, "A new pulsed wave Doppler ultrasound system to measure blood velocities beyond the Nyquist limit," *IEEE Trans. Ultrason., Ferroelectr., Freq. Control*, vol. 42, no. 2, pp. 265–279, Mar. 1995, doi: 10.1109/58.365240.

[24] M. Mozumi, R. Nagaoka, M. Cinthio, and H. Hasegawa, "Anti-aliasing method for ultrasonic 2D phase-sensitive motion estimator," *Jpn. J. Appl. Phys.*, vol. 59, no. SK, May 2020, Art. no. SKKE20, doi: 10.35848/1347-4065/ab8c9a.

[25] J. Poree *et al.*, "Dealiasing high-frame-rate color Doppler using dual-wavelength processing," *IEEE Trans. Ultrason., Ferroelectr., Freq. Control*, vol. 68, no. 6, pp. 2117–2128, Jun. 2021, doi: 10.1109/TUFFC.2021.3056932.

[26] Y. Obara, S. Mori, M. Arakawa, and H. Kanai, "Multifrequency phased tracking method for estimating velocity in heart wall," *Ultrasound Med. Biol.*, vol. 47, no. 4, pp. 1077–1088, Apr. 2021, doi: 10.1016/j.ultrasmedbio.2020.12.011.

[27] Y. Obara, S. Mori, M. Arakawa, and H. Kanai, "Strain rate distribution in layered myocardium measured using local velocity estimator with multifrequency phase differences," *Ultrasound Med. Biol.*, vol. 47, no. 9, pp. 2768–2773, Sep. 2021, doi: 10.1016/j.ultrasmedbio.2021.05.021.

[28] H. Hasegawa and H. Kanai, "Modification of the phased-tracking method for reduction of artifacts in estimated artery wall deformation," *IEEE Trans. Ultrason., Ferroelectr., Freq. Control*, vol. 53, no. 11, pp. 2050–2064, Nov. 2006, doi: 10.1109/TUFFC.2006.145.

[29] A. P. G. Hoeks, T. G. J. Arts, P. J. Brands, and R. S. Reneman, "Comparison of the performance of the RF cross correlation and Doppler autocorrelation technique to estimate the mean velocity of simulated ultrasound signals," *Ultrasound Med. Biol.*, vol. 19, no. 9, pp. 727–740, 1993, doi: 10.1016/0301-5629(93)90090-B.

[30] Y. Honjo, H. Hasegawa, and H. Kanai, "Optimization of correlation kernel size for accurate estimation of myocardial contraction and relaxation," *Jpn. J. Appl. Phys.*, vol. 51, Jul. 2012, Art. no. 07GF06, doi: 10.1143/JJAP.51.07GF06.

[31] I. J. LeGrice, B. H. Smaill, L. Z. Chai, S. G. Edgar, J. B. Gavin, and P. J. Hunter, "Laminar structure of the heart: Ventricular myocyte arrangement and connective tissue architecture in the dog," *Amer. J. Physiol.-Heart Circulatory Physiol.*, vol. 269, no. 2, pp. H571–H582, Aug. 1995, doi: 10.1152/ajpheart.1995.269.2.H571.

[32] H. Hasegawa and H. Kanai, "High-frame-rate echocardiography using diverging transmit beams and parallel receive beamforming," *J. Med. Ultrason.*, vol. 38, no. 3, pp. 129–140, 2011, doi: 10.1007/s10396-011-0304-0.

[33] F. J. Harris, "On the use of windows for harmonic analysis with the discrete Fourier transform," *Proc. IEEE*, vol. 66, no. 1, pp. 51–83, Jan. 1978, doi: 10.1109/PROC.1978.10837.

[34] A. H. Nuttall, "Some windows with very good sidelobe behavior," *IEEE Trans. Acoust., Speech, Signal Process.*, vol. ASSP-29, no. 1, pp. 84–91, Feb. 1981, doi: 10.1109/TASSP.1981.1163506.

[35] C. Papadacci, M. Pernot, M. Couade, M. Fink, and M. Tanter, "High-contrast ultrafast imaging of the heart," *IEEE Trans. Ultrason., Ferroelectr., Freq. Control*, vol. 61, no. 2, pp. 288–301, Feb. 2014, doi: 10.1109/TUFFC.2014.6722614.

[36] J. Grondin, V. Sayseng, and E. E. Konofagou, "Cardiac strain imaging with coherent compounding of diverging waves," *IEEE Trans. Ultrason., Ferroelectr., Freq. Control*, vol. 64, no. 8, pp. 1212–1222, Aug. 2017, doi: 10.1109/TUFFC.2017.2717792.

[37] L. Tong, H. Gao, H. F. Choi, and J. D'hooge, "Comparison of conventional parallel beamforming with plane wave and diverging wave imaging for cardiac applications: A simulation study," *IEEE Trans. Ultrason., Ferroelectr., Freq. Control*, vol. 59, no. 8, pp. 1654–1663, Aug. 2012, doi: 10.1109/TUFFC.2012.2371.

[38] P. Palka, A. Lange, A. D. Fleming, G. R. Sutherland, L. N. Fenn, and W. N. McDicken, "Doppler tissue imaging: Myocardial wall motion velocities in normal subjects," *J. Amer. Soc. Echocardiogr.*, vol. 8, no. 5, pp. 659–668, Sep.-Oct. 1995, doi: 10.1016/S0894-7317(05)80380-3.

[39] H. Dalen, A. Thorstensen, L. J. Vatten, S. A. Aase, and A. Stoylen, "Reference values and distribution of conventional echocardiographic Doppler measures and longitudinal tissue Doppler velocities in a population free from cardiovascular disease," *Circulation, Cardiovascular Imag.*, vol. 3, no. 5, pp. 614–622, Sep. 2010, doi: 10.1161/CIRCIMAGING.109.926022.

[40] J. Koyama, P. A. Ray-Sequin, and R. H. Falk, "Longitudinal myocardial function assessed by tissue velocity, strain, and strain rate tissue Doppler echocardiography in patients with AL (primary) cardiac amyloidosis," *Circulation*, vol. 107, no. 19, pp. 2446–2452, May 2003, doi: 10.1161/01.CIR.0000068313.67758.4F.

[41] J. Grondin, D. Wang, C. S. Grubb, N. Trayanova, and E. E. Konofagou, "4D cardiac electromechanical activation imaging," *Comput. Biol. Med.*, vol. 113, Oct. 2019, Art. no. 103382, doi: 10.1016/j.compbiomed.2019.103382.

[42] V. Sayseng *et al.*, "Catheter ablation lesion visualization with intracardiac strain imaging in canines and humans," *IEEE Trans. Ultrason., Ferroelectr., Freq. Control*, vol. 67, no. 9, pp. 1800–1810, Sep. 2020, doi: 10.1109/TUFFC.2020.2987480.

[43] Y. Notomi *et al.*, "Measurement of ventricular torsion by two-dimensional ultrasound speckle tracking imaging," *J. Amer. College Cardiol.*, vol. 45, no. 12, pp. 2034–2041, Jun. 2005.

[44] S. Langeland *et al.*, "Experimental validation of a new ultrasound method for the simultaneous assessment of radial and longitudinal myocardial deformation independent of insonation angle," *Circulation*, vol. 112, no. 14, pp. 2157–2162, Oct. 2005, doi: 10.1161/CIRCULATIONAHA.105.554006.

[45] K. Saito *et al.*, "Comprehensive evaluation of left ventricular strain using speckle tracking echocardiography in normal adults: Comparison of three-dimensional and two-dimensional approaches," *J. Amer. Soc. Echocardiography*, vol. 22, no. 9, pp. 1025–1030, Sep. 2009, doi: 10.1016/j.echo.2009.05.021.

[46] H. Hasegawa, "Phase-sensitive 2D motion estimators using frequency spectra of ultrasonic echoes," *Appl. Sci.*, vol. 6, no. 7, pp. 1–19, Apr. 2016, doi: 10.3390/app6070195.

[47] S. Nunome, R. Nagaoka, and H. Hasegawa, "Accuracy evaluation of 3D velocity estimation by multi-frequency phase-sensitive motion estimator under various specifications of matrix array probe," *Jpn. J. Appl. Phys.*, vol. 59, no. SK, Jul. 2020, Art. no. SKKE01, doi: 10.35848/1347-4065/ab78e7.

Yu Obara was born in Iwate, Japan, in August 1996. He received the B.S. degree in electrical engineering and the M.S. degree in biomedical engineering from Tohoku University, Sendai, Japan, in 2019 and 2021, respectively, where he is currently pursuing the Ph.D. degree in biomedical engineering.

His research interests include transcutaneous measurements of the heart wall vibrations and myocardial response to propagation of electrical potential.

Mr. Obara is a member of the Acoustical Society of Japan and the Japan Society of Ultrasonics in Medicine.

Shohei Mori (Member, IEEE) was born in Miyazaki, Japan, in February 1991. He received the B.S., M.S., and Ph.D. degrees in engineering from the Tokyo Institute of Technology, Tokyo, Japan, in 2013, 2015, and 2017, respectively.

Since 2017, he has been an Assistant Professor with the Department of Electrical Engineering, Graduate School of Engineering, Tohoku University, Sendai, Japan. His research interests include ultrasound measurements of organ dynamics for cardiovascular diseases and quantification of the amplitude envelope statistics for tissue characterization of liver diseases.

Dr. Mori is a member of the Acoustical Society of Japan and an Engineering Fellow of the Japan Society of Ultrasonics in Medicine.

Mototaka Arakawa (Member, IEEE) was born in Sendai, Japan, in January 1971. He received the B.S., M.S., and Ph.D. degrees in electrical engineering from Tohoku University, Sendai, Japan, in 1993, 1995, and 2000, respectively.

He is currently an Associate Professor with the Graduate School of Biomedical Engineering, Tohoku University. His research interests include viscoelasticity measurements of biological tissues and the development of acoustic microscopy for tissue and cell characterization.

Dr. Arakawa is a member of the Acoustical Society of Japan, the Japan Society of Ultrasonics in Medicine, and the Institute of Electronics Information and Communication Engineering of Japan.

Hiroshi Kanai (Senior Member, IEEE) was born in Matsumoto, Japan, in November 1958. He received the B.E., M.E., and Ph.D. degrees in electrical engineering from Tohoku University, Sendai, Japan, in 1981, 1983, and 1986, respectively.

From 1986 to 1988, he was a Research Associate with the Education Center for Information Processing, Tohoku University. From 1990 to 1992, he was a Lecturer with the Department of Electrical Engineering, Faculty of Engineering, Tohoku University. From 1992 to 2001, he was an Associate Professor with the Department of Electrical Engineering, Faculty of Engineering, Tohoku University. From 2012 to 2015, he was the Dean of the Graduate School of Engineering, Tohoku University, where he was the Vice President of research consolidation and university reform from 2015 to 2018. Since 2001, he has been a Professor with the Department of Electronic Engineering, Graduate School of Engineering, Tohoku University, where he has also been a Professor with the Department of Biomedical Engineering, Graduate School of Biomedical Engineering, since 2008. His present interests are in transcutaneous measurement of the heart wall vibrations and myocardial response to propagation of electrical potential and cross-sectional imaging of elasticity around atherosclerotic plaque with transcutaneous ultrasound for tissue characterization of the arterial wall.

Dr. Kanai is a member of the Acoustical Society of Japan, a fellow of the Institute of Electronics Information and Communication Engineering of Japan, and a member of the Japan Society of Ultrasonics in Medicine, the Japan Society of Medical Electronics and Biological Engineering, and the Japanese Circulation Society. Since 1998, he has been a member of the Technical Program Committee of the IEEE Ultrasonics Symposium. Since 2011, he has been a Board Member of the International Congress on Ultrasonics. Since 2013, he has been an Associate Editor of the IEEE TRANSACTIONS ON ULTRASONICS, FERROELECTRICS, AND FREQUENCY CONTROL. He was an Editor of the *Journal of Medical Ultrasonics* and the *Japanese Journal of Medical Ultrasonics* from 2012 to 2018.